International Journal of Heat and Mass Transfer 274 (2027) 129844

Contents lists available at ScienceDirect

International Journal of Heat and Mass Transfer

journal homepage: www.elsevier.com/locate/ijhmt

Effectively manipulating phonon thermal transport across large-scale nanostructured interfaces via tailoring interface roughness

Xin Ran [a,*], Bingyang Cao [b,*]

[a] Ministry of Education Key Laboratory of NSLSCS, Phonon Engineering Research Center of Jiangsu Province, Center for Quantum Transport and Thermal Energy Science, Institute of Physics Frontiers and Interdisciplinary Sciences, School of Physics and Technology, Nanjing Normal University, Nanjing 210023, China
[b] Key Laboratory of Thermal Science and Power Engineering of Education of Ministry, Department of Engineering Mechanics, Tsinghua University, Beijing 100084, China

ARTICLE INFO

Keywords:
Interfacial phonon transport
Thermal conductivity
Nanostructured interface
Interface roughness
Monte Carlo method

ABSTRACT

Although previous researchers have found that large-scale nanostructured interfaces can facilitate interfacial phonon transport, their further optimization remains elusive. Past studies mainly focused on the role of geometry yet rarely considered the interface roughness. Herein, we report a significant impact of interface roughness on this manipulation, and develop a semiquantitative strategy to further optimize phonon thermal transport across such interface. The present work shows distinct trends of thermal conductivity in bilayer films with varying vertical and horizontal interface roughnesses. Meanwhile, it confirms that large-scale nanostructured interfaces can facilitate interfacial phonon transport at various interface roughnesses, when compared with the planar interface at the same roughness as their vertical interfaces. Nevertheless, compared with optimal thermal conductivity for planar interface throughout the entire roughness range, large-scale nanostructured interfaces can either facilitate or suppress interfacial phonon transport. Without loss of generality, one large-scale nanostructured interface is simulated across full matrix of roughness combination to identify the optimal combination for maximizing thermal conductivity. The current manipulation arises from the combined effect induced by large-scale nanostructured interfaces, including transmission probability, extra thermal resistance in heat flux direction, contact area and phonon trajectory redirection. These phenomena are dictated by interface transmissivity, interfacial scattering mechanism, additional thermal conduction pathway and multiple coupled interfacial scattering events, respectively. Based on this combined effect, to maximize thermal conductivity, a specific roughness achieving near-maximal overall interface transmissivity is recommended for vertical interfaces. Whereas horizontal interfaces require another specific roughness that can induce partially specular and partially diffuse interfacial scattering to redirect the trajectories of backward phonons, and prevent excessive resistive scattering.

1. Introduction

In past several decades, micro/nanoscale phonon thermal transport attracts increasing attentions owing to its important applications in thermal management of micro/nanoelectronics and optimization of thermoelectrics [1,2]. Since interfaces widely exist in these devices with nonnegligible contributions to phonon thermal transport, the manipulation of interfacial phonon transport is crucial for the thermal management and optimization of these devices [3–5]. However, the classical law, Fourier's law, may fail at micro/nanoscale, hence it is urgent to develop novel theories and methods to manipulate interfacial phonon transport [6,7].

Previous researchers have found that nanostructured interfaces can manipulate interfacial phonon transport [8–10]. Molecular dynamics method was taken to simulate phonon thermal transport across nanostructured interface and first revealed the promotion of interfacial phonon transport by nanostructured interface [8]. The relationship between thermal boundary conductance and characteristic size was constructed for nanostructured interfaces by molecular dynamics method [11]. The size of nanostructured interface was optimized to maximize interfacial phonon transport by combining theoretical and molecular dynamics methods [12]. The impact of the nanostructured interface shape on interfacial phonon transport was revealed through combining lattice Boltzmann and molecular dynamics methods [13]. Other

* Corresponding authors.
E-mail addresses: ranxin25@njnu.edu.cn (X. Ran), caoby@tsinghua.edu.cn (B. Cao).

https://doi.org/10.1016/j.ijheatmasstransfer.2026.129844
Received 30 July 2026; Received in revised form 25 October 2026; Accepted 2 November 2026
0017-9310/© 2026 Elsevier Ltd. All rights are reserved, including those for text and data mining, AI training, and similar technologies.

experiments and simulations also demonstrated the nanostructured interface could enhance interfacial phonon transport [14–17]. Above works attributed the enhancement of interfacial phonon transport by nanostructured interface to the additional thermal conduction pathway via increasing interface area [12,13,15,16]. However, some experiments observed the reduction of interfacial phonon transport after increasing interface area by replacing the planar interface with nanostructured interface [10]. The nanostructured interface was also found to reduce interfacial phonon transport at various interface geometries by Monte Carlo method [9]. To resolve the contradictory conclusion, the interface roughness was introduced and the interfaces were further classified into small-scale and large-scale nanostructured types, with characteristic sizes much smaller than and on the order of phonon mean free paths, respectively. Small-scale nanostructured interfaces were found to enhance and reduce interfacial phonon transport at small and large interface roughnesses, respectively [18]. Conversely, large-scale nanostructured interfaces were demonstrated to universally enhance interfacial phonon transport [18]. Furthermore, at small-scale nanostructured interface, part studies highlighted the significant impact of interface roughness and geometry on the manipulation of interfacial phonon transport and offered the corresponding optimization strategies [9,18]. In contrast, at large-scale nanostructured interface, prior works attributed its promotion for interfacial phonon transport solely to additional thermal conduction pathway and provided the optimization strategy based primarily on geometry [11–13]. In reality, the small size of small-scale nanostructured interfaces limits additional thermal conduction pathways and makes single interfacial scattering the primary scattering process. With increasing size, the impact of geometry becomes increasingly strong, and thus compared with small-scale counterparts, large-scale nanostructured interfaces open more additional thermal conduction pathways and result in more multiple coupled interfacial scattering events. Through enhanced multiple coupled interfacial scattering events, the interface roughness and additional thermal conduction pathway synergistically impact phonon thermal transport across large-scale nanostructured interface. Therefore, it is necessary to elucidate this synergistic impact and develop the corresponding optimization strategy for such interface.

When a phonon is incident on the interface, it will transmit through the interface or be reflected with the probability for transmission defined as the interface transmissivity. Three classical interface models were developed to calculate the interface transmissivity, namely acoustic mismatch model (AMM) [19], diffuse mismatch model (DMM) [20] and mixed mismatch model (MMM) [21]. AMM was developed based on the assumption of phonons equivalent to plane waves, working better at fully smooth interface or low temperature where phonons are completely specularly scattered [19]. DMM was developed based on the assumption of phonons equivalent to particles, working better at fully rough interface or high temperature where phonons are completely diffusely scattered [20]. MMM was developed based on partially specular and partially diffuse interfacial scattering, where phonons are neither completely equivalent to plane waves nor particles. The probability of specular interfacial scattering is quantified by the specularity, related to the interface roughness [21]. These interface models regarded the interface transmissivity and specularity as constants [19–21]. However, both theoretical calculations and experiments reveal the strong frequency-dependence of the interface transmissivity and specularity [22,23]. Then interface models were developed to partially include the effects of spectral specularity, spectral specular scattering and spectral diffuse scattering, working well in predicting the measured thermal boundary conductance or interface transmissivity [24–27]. Recently, starting from the principle of detailed balance at interface, an interface model was developed to simultaneously consider the effects of spectral specularity, spectral specular scattering and spectral diffuse scattering, called spectral mixed mismatch model (SMMM). This model predicts the thermal boundary conductance and interface transmissivity from theoretical calculations and experiments better [18]. Hence SMMM will be adopted to investigate the impact of interface roughness on interfacial phonon transport across large-scale nanostructured interface in present work.

The methods for interfacial phonon transport mainly include microscopic methods, mesoscopic methods and experiments. Microscopic methods are commonly used in small systems while highly computational consuming in large systems [28,29]. Experiments are difficult for detailed analyses of the underlying mechanisms in interfacial phonon transport [30,31]. Based on phonon Boltzmann transport equation, mesoscopic methods is applied in large systems, containing deterministic methods and Monte Carlo method (MC) [21,32]. As one of deterministic methods, discrete ordinates method (DOM) is highly efficient in simulations for simple geometry yet difficult to handle complex geometry [33]. MC takes the random sampling technique to solve phonon Boltzmann transport equation with large noise errors yet can handle the complex geometry easily [9]. MC is adopted in present work owing to the complex geometry of nanostructured interface. MCs for gray interface transmissivity [34] and gray interface transmissivity and specularity [35] was constructed in sequence. Then the effects of spectral specularity, spectral specular scattering and spectral diffuse scattering were partially considered at homogeneous or heterogeneous interface in MC [9,36]. Recently, MC simultaneously considering the effects of spectral specularity, spectral specular scattering and spectral diffuse scattering was developed at heterogeneous interface [18], which is applied to study the impact of interface roughness on interfacial phonon transport across nanostructured interface here.

Herein, this work focuses on interfacial phonon transport across large-scale nanostructured interface with characteristic size on the order of phonon mean free paths, and aims to investigate the impact of interface roughness and demonstrate a semiquantitative strategy to manipulate phonon thermal transport. The rest of this paper is organized as follow: First, Section 2 introduces the theoretical basis and numerical method, consisted of phonon Boltzmann transport equation and phonon Monte Carlo method; then, the numerical method is validated in monolayer and bilayer films in Section 3 through comparisons with discrete ordinates method and experiment; next, the detailed results and discussions are presented in Section 4, containing those for varying the horizontal and vertical roughnesses uniformly and nonuniformly in subsections 4.1 and 4.2, respectively, and the optimal interface roughnesses in subsection 4.3; finally, Section 5 provides the total conclusion.

2. Theoretical basis and numerical method

This section will introduces the theoretical basis and numerical framework of Monte Carlo method in present work.

2.1. Phonon Boltzmann transport equation

Phonon Boltzmann transport equation gives the evolution law of phonon distribution with time, space and momentum as below [32]

$$\frac{\partial f}{\partial t}+\mathbf{v}_{\mathrm{g}}(\omega,\mathrm{p})\cdot\nabla f=\frac{f^{\mathrm{pse}}-f}{\tau(\omega,\mathrm{p},T)}, \tag{1}$$

with phonon distribution f, Bose-Einstein distribution f^{pse} at pseudo-equilibrium temperature T^{pse}, and group velocity $\mathbf{v}_{\mathrm{g}}$ and relaxation time τ at frequency ω and polarization p. Introducing phonon equilibrium distribution f^{ref} at reference equilibrium temperature T^{ref}, Eq. (1) can be rewritten as [32]

$$\frac{\partial f^{\mathrm{d}}}{\partial t}+\mathbf{v}_{\mathrm{g}}(\omega,\mathrm{p})\cdot\nabla f^{\mathrm{d}}=\frac{\left(f^{\mathrm{pse}}-f^{\mathrm{ref}}\right)-f^{\mathrm{d}}}{\tau(\omega,\mathrm{p},T)}, \tag{2}$$

with deviational phonon distribution $f^{\mathrm{d}}=f-f^{\mathrm{ref}}$. By multiplying $\hbar\omega$ at both sides with reduced Plank constant $\hbar$, Eq. (2) can be rewritten as [32]

$$\frac{\partial e^{\mathrm{d}}}{\partial t}+\mathbf{v}_{\mathrm{g}}(\omega,\mathrm{p})\cdot\nabla e^{\mathrm{d}}=\frac{\left(e^{\mathrm{pse}}-e^{\mathrm{ref}}\right)-e^{\mathrm{d}}}{\tau(\omega,\mathrm{p},T)}, \tag{3}$$

with phonon energy distribution $e=\hbar\omega f^{\mathrm{d}}$, pseudo-equilibrium energy distribution $e^{\mathrm{pse}}=\hbar\omega f^{\mathrm{pse}}$ and reference equilibrium energy distribution $e^{\mathrm{ref}}=\hbar\omega f^{\mathrm{ref}}$. Kinetic-type Monte Carlo method (KMC) considers phonon transport under small temperature difference, where Eq. (3) can be approximately linearized as [32]

$$\frac{\partial e^{\mathrm{d}}}{\partial t}+\mathbf{v}_{\mathrm{g}}(\omega,\mathrm{p})\cdot\nabla e^{\mathrm{d}}=\frac{\hbar\omega\left(T^{\mathrm{pse}}-T^{\mathrm{ref}}\right)\left.\frac{\mathrm{d}f^{\mathrm{ref}}}{\mathrm{d}T}\right|_{T^{\mathrm{ref}}}-e^{\mathrm{d}}}{\tau\left(\omega,\mathrm{p},T^{\mathrm{ref}}\right)}. \tag{4}$$

Further simplifying Eq. (4) at steady state, the theoretical basis of steady-state kinetic-type Monte Carlo method (SKMC), which is introduced in subsection 2.2, can be obtained as [32,37]

$$\mathbf{v}_{\mathrm{g}}(\omega,\mathrm{p})\cdot\nabla e^{\mathrm{d}}=\frac{\hbar\omega\left(T^{\mathrm{pse}}-T^{\mathrm{ref}}\right)\left.\frac{\mathrm{d}f^{\mathrm{ref}}}{\mathrm{d}T}\right|_{T^{\mathrm{ref}}}-e^{\mathrm{d}}}{\tau\left(\omega,\mathrm{p},T^{\mathrm{ref}}\right)}. \tag{5}$$

2.2. Phonon Monte Carlo method

By random sampling technique and statistical simulation, phonon MC can solve phonon Boltzmann transport equation to obtain the temperature and heat flux distributions in systems. SKMC, an extended version of KMC, avoids the simulation of phonon transient transport process and directly calculates the steady-state temperature and heat flux [32,37,38]. It tracks random walks of all energy packets one by one under small temperature difference. The track for each energy packet undergoes five steps, containing initialization, advection, scattering, sampling and boundary treatment, with detailed algorithms in Refs. [37, 38]. One energy packet is first initialized by determining its frequency, polarization, group velocity, moving direction and relaxation time, and then emitted from isothermal boundary. Next it advects within the system, during which it is scattered and simultaneously contributes to the sampling of steady-state temperature and heat flux. Finally its track is terminated when it encounters the isothermal boundary. Three scatterings are considered in present work, i.e. intrinsic, boundary and interfacial scatterings. The former two are implemented according to Refs. [37,38], and the last one follows the formulation referred to Ref. [18]. For interfacial scattering, partially specular and partially diffuse scattering is simulated at various interface roughnesses based on spectral mixed mismatch model (SMMM) in present work. In SMMM, the interface transmissivity is calculated by the formulas below [18]

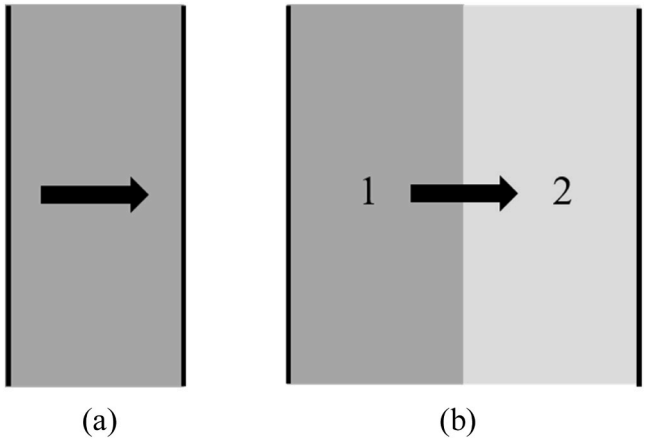


Fig. 1. Schematic diagrams of physical models for validations: (a) monolayer film and (b) bilayer film.

$$\begin{aligned}\alpha_{12}(\theta_1,\omega,\mathrm{p})&=P_1(\omega,\mathrm{p})\alpha_{\mathrm{Specular},12}(\theta_1,\omega,\mathrm{p})+(1-P_1(\omega,\mathrm{p}))\alpha_{\mathrm{Diffuse},12}(\omega,\mathrm{p})\\&=\exp\left(-\frac{16\pi^2\eta^2}{\lambda_1^2(\omega,\mathrm{p})}\right)\cdot\min\left\{1,\frac{P_2(\omega,\mathrm{p})C_{\omega,\mathrm{p},2}v_{\mathrm{g},2}^3(\omega,\mathrm{p})}{P_1(\omega,\mathrm{p})C_{\omega,\mathrm{p},1}v_{\mathrm{g},1}^3(\omega,\mathrm{p})}\right\}\frac{\frac{4\rho_2 v_{\mathrm{g},2}(\omega,\mathrm{p})}{\rho_1 v_{\mathrm{g},1}(\omega,\mathrm{p})}\frac{\cos\theta_2}{\cos\theta_1}}{\left(\frac{\rho_2 v_{\mathrm{g},2}(\omega,\mathrm{p})}{\rho_1 v_{\mathrm{g},1}(\omega,\mathrm{p})}+\frac{\cos\theta_2}{\cos\theta_1}\right)^2},\\&+\left(1-\exp\left(-\frac{16\pi^2\eta^2}{\lambda_1^2(\omega,\mathrm{p})}\right)\right)\cdot\frac{(1-P_2(\omega,\mathrm{p}))k_2^2(\omega,\mathrm{p})}{(1-P_1(\omega,\mathrm{p}))k_1^2(\omega,\mathrm{p})+(1-P_2(\omega,\mathrm{p}))k_2^2(\omega,\mathrm{p})}\end{aligned} \tag{6}$$

$$\begin{aligned}\alpha_{21}(\theta_2,\omega,\mathrm{p})&=P_2(\omega,\mathrm{p})\alpha_{\mathrm{Specular},21}(\theta_2,\omega,\mathrm{p})+(1-P_2(\omega,\mathrm{p}))\alpha_{\mathrm{Diffuse},21}(\omega,\mathrm{p})\\&=\exp\left(-\frac{16\pi^2\eta^2}{\lambda_2^2(\omega,\mathrm{p})}\right)\cdot\min\left\{1,\frac{P_1(\omega,\mathrm{p})C_{\omega,\mathrm{p},1}v_{\mathrm{g},1}^3(\omega,\mathrm{p})}{P_2(\omega,\mathrm{p})C_{\omega,\mathrm{p},2}v_{\mathrm{g},2}^3(\omega,\mathrm{p})}\right\}\frac{\frac{4\rho_2 v_{\mathrm{g},2}(\omega,\mathrm{p})}{\rho_1 v_{\mathrm{g},1}(\omega,\mathrm{p})}\frac{\cos\theta_2}{\cos\theta_1}}{\left(\frac{\rho_2 v_{\mathrm{g},1}(\omega,\mathrm{p})}{\rho_1 v_{\mathrm{g},1}(\omega,\mathrm{p})}+\frac{\cos\theta_2}{\cos\theta_1}\right)^2},\\&+\left(1-\exp\left(-\frac{16\pi^2\eta^2}{\lambda_2^2(\omega,\mathrm{p})}\right)\right)\cdot\frac{(1-P_1(\omega,\mathrm{p}))k_1^2(\omega,\mathrm{p})}{(1-P_1(\omega,\mathrm{p}))k_1^2(\omega,\mathrm{p})+(1-P_2(\omega,\mathrm{p}))k_2^2(\omega,\mathrm{p})}\end{aligned} \tag{7}$$

with incident angles at interface from material 1–2 being θ_1 and from material 2–1 being θ_2, spectral specularity P, spectral volume heat capacity $C_\omega=\hbar\omega D(\omega,\mathrm{p})\left.\frac{\mathrm{d}f}{\mathrm{d}T}\right|_{T^{\mathrm{ref}}}$ with density of states $D(\omega,\mathrm{p})$, transmissivities from material 1–2 for spectral specular scattering being $\alpha_{\mathrm{Specular},12}$ and spectral diffuse scattering being $\alpha_{\mathrm{Diffuse},12}$, transmissivities from material 2–1 for spectral specular scattering being $\alpha_{\mathrm{Specular},21}$ and spectral diffuse scattering being $\alpha_{\mathrm{Diffuse},21}$, phonon wavelength λ, phonon wave number k and interface roughness η. SMMM cannot only account for the spectrum dependence of specularity, specular scattering and diffuse scattering but also satisfy the principle of detailed balance. Although inelastic scattering and mode conversion are neglected at interface, SMMM is still the most appropriate theoretical interface model for spectral specularity and spectral transmissivity [18]. Thus it is adopted to calculate the interface transmissivity in SKMC. To implement interfacial scattering, the distances from the current location of one energy packet to the positions of intrinsic, boundary and interfacial scattering events are calculated. Interfacial scattering will occur when the distance for interfacial scattering event is shortest. Two random numbers are generated and one of them is compared with the specularity to determine whether the energy packet is scattered specularly or diffusely, and then the other is compared with the spectral transmissivity for specular scattering or diffuse scattering to determine whether the energy packet transmits the interface or is reflected. The specularly scattered energy packets follow Snell's law whereas the diffusely scattered energy packets follow Lambert's cosine law. The frequency and mode are fixed for both transmitted and reflected energy packets. The group velocity and relaxation time are updated based on phonon dispersions on the new side for transmitted ones whereas not changed for reflected ones. The detailed implementations for interfacial scattering are referred to Ref. [18].

3. Validations

SKMC is validated in this section through comparisons with discrete ordinates method and experiment in monolayer and bilayer films.

3.1. Monolayer films

In this subsection, monolayer films made of Al, Si and Ge are simulated using SKMC in Section 2, shown in Fig. 1. The isotropic phonon dispersions along [100] direction of Al, Si and Ge are referred from Refs. [39–41], with both acoustic and optical modes. For Al, the phonon

relaxation times are assumed to be constant at all phonon frequencies and polarizations under each temperature, and only the contribution from phonons is present and that from electrons is neglected [42]. With the lattice thermal conductivities at various temperatures in Ref. [43], the constants are calculated based on the relationship between the lattice thermal conductivity and relaxation time below [32]

$$\kappa = \frac{1}{3}\sum_{\mathrm{p}} \int C_\omega v_{\mathrm{g}}^2(\omega, \mathrm{p})\tau d\omega. \tag{8}$$

The left and right boundaries of all films are fixed at equilibrium temperatures $T_{\mathrm{L}} = 303$ K and $T_{\mathrm{R}} = 297$ K, and the total thickness increases from 20 to 100 nm with the common difference 20 nm and from 100 to 500 nm with the common difference 50 nm. The total number of energy packets is selected as 120,000,000 for all simulations after comprehensively considering the computational assumption and noise error in SKMC. The steady-state temperature distributions and heat fluxes at various total thicknesses are directly obtained by SKMC. Then the thermal conductivity is calculated based on Fourier's law through formula, $\kappa = q/(L(T_{\mathrm{L}} - T_{\mathrm{R}}))$, with heat flux q and total thickness L. The temperature distributions and thermal conductivities obtained by SKMC are compared with the well-developed discrete ordinates method (DOM) in Refs. [44,45], shown in Fig. 2. Good agreements are found between SKMC and DOM, verifying the present SKMC even though the thermal conductivity calculation has not converged due to the strong boundary scattering. Thus the present SKMC can accurately capture the intrinsic and boundary scatterings, and simulate phonon transport in monolayer films. Furthermore, the temperature jump at boundary is found to increase with decreasing the total thickness, caused by the enhanced non-equilibrium effect due to the intensified boundary scattering. Correspondingly, the thermal conductivity is found to decrease with decreasing the total thickness, indicating an increase in thermal resistance at boundary resulted from the intensified boundary scattering.

3.2. Bilayer films

In this subsection, bilayer films made of Al(1)/Si(2) and Ge(1)/Si(2) are simulated using SKMC in Section 2, shown in Fig. 1, which are first compared with the recent DOM in Ref. [33]. The phonon dispersions and relaxation times of Al, Si and Ge are identical to those in Section 3.1. The left and right boundary temperatures are fixed at 303 and 297 K, and two cases are considered here, i.e. changing total thickness whereas fixing interface roughness and changing interface roughness whereas fixing total thickness. For the first case, the total thickness increases from 20 to 100 nm with the common difference 20 nm and then from 100 to 500 nm with the common difference 50 nm, where the interface roughness and material ratio are all fixed at 0.15 nm and 1. For the second case, the interface roughness increases from 0.02 to 0.2 nm with the common difference 0.02 nm and from 0.2 to 1.8 nm with the common difference 0.2 nm, where the total thickness and material ratio are all fixed at 100 nm and 1. In all simulations, the total number of energy packets is fixed at 300,000,000 after the comprehensive consideration for the computational assumption and noise error, and the spatial steps to sample the temperature are fixed at 0.01 nm. The temperature jump

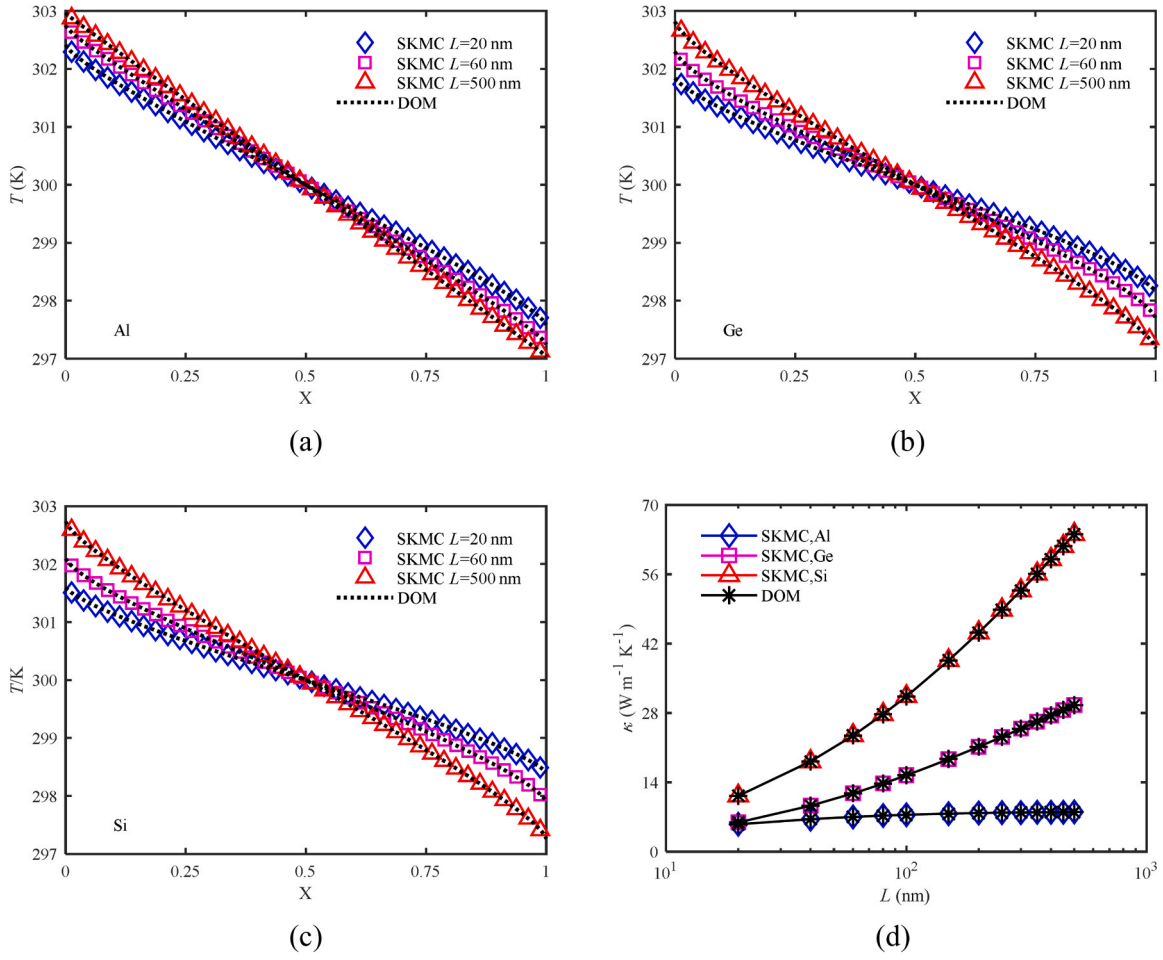


Fig. 2. The steady-state temperature distribution and thermal conductivity at various thicknesses of monolayer films: (a) the steady-state temperature distribution of Al film, (b) the steady-state temperature distribution of Ge film, (c) the steady-state temperature distribution of Si film and (d) thermal conductivity of Al, Ge and Si films.

at interface is obtained by fitting the steady-state temperature distributions on both sides of interface using the quartic polynomial below

$$T = A_0 + A_1 \mathrm{X} + A_2 \mathrm{X}^2 + A_3 \mathrm{X}^3 + A_4 \mathrm{X}^4, \tag{9}$$

with the dimensionless position $\mathrm{X} = x/L$ and fitting parameters A_0, A_1, A_2 and A_4. After obtaining temperature jumps and heat fluxes, the thermal boundary conductances are calculated by formula, $G = q/\Delta T$, with heat flux q and temperature jump ΔT at interfaces. The quartic polynomial is demonstrated to be a good fit to the simulation results, with two examples shown in Fig. 3. The comparisons between SKMC and DOM are given in Fig. 4 and Fig. 5 for temperature distributions and thermal boundary conductances, respectively, showing good agreements. It should be noted that the thermal boundary conductance is underestimated due to the neglect of the electronic contribution, inelastic scattering and mode conversion [46]. Thus the present SKMC is verified to accurately capture interfacial scattering and simulate interfacial phonon transport in bilayer films. Furthermore, the temperature jump at interface is found to increase with decreasing the total thickness, caused by the enhanced non-equilibrium effect due to the intensified interfacial scattering. Correspondingly, the thermal boundary conductance is found to decrease with decreasing the total thickness, indicating increasing thermal resistance at interface resulted from the intensified interfacial scattering.

Secondly, the bilayer films made of Al/Si are simulated using the present SKMC to compare thermal boundary conductance with experiment in Refs. [47,48]. Since lattice thermal conductivity is only available at five temperatures, namely, 100, 150, 200, 250 and 300 K, the thermal boundary conductances are calculated under these reference temperatures. Left and right boundary temperature differences are set around the reference temperatures to ensure the validity of small temperature difference assumption. The thickness of Al is set as 100 nm, identical with experiment, and the thickness of Si substrate is set as 1000 nm to ensure to be much larger than mean free paths of phonons in Si and simultaneously avoid significant computational cost. All spatial steps are the same as the above simulations. For interface roughness, the interface was high-quality due to the removal of its natural oxide, mentioned in the experiment; however, the specific value was not given [48]. Thus referred to the measured interface roughness by transmission electron microscopy [49], the interface roughnesses are selected as 0 nm, 0.02 nm, 0.04 nm, 0.06 nm, 0.3 nm and infinity in simulation, where 0 nm and infinity characterize fully smooth and fully rough interfaces, respectively. The thermal boundary conductances are calculated by the same approach above using steady-state temperature distributions and heat fluxes, shown in Fig. 6. Although the neglect of electronic contribution, inelastic scattering and mode conversion result in the underestimation of thermal boundary conductance [46], good agreements are found in the thermal boundary conductances by SKMC and experiment. Furthermore, the deviation of SKMC from experiment is smaller and smaller with decreasing interface roughness, indicating it can well capture the interfacial scattering in reality. Totally, through all comparisons with discrete ordinates method and experiment, the present SKMC has been validated and subsequently applied to investigate phonon transport through nanostructured interfaces.

4. Results and discussions

In this section, phonon thermal transport across large-scale nanostructured interface is investigated by SKMC at various interface roughnesses. Each nanostructured interface consists of two types of interfaces, i.e. the horizontal and vertical interfaces, parallel and perpendicular to the heat flux direction, respectively. Uniform and nonuniform interface roughnesses are first considered successively, corresponding to the two cases where the interface roughness of horizontal interfaces is equal and unequal to that of vertical interfaces, respectively. Then the optimal interface roughness combinations are obtained and a semiquantitative manipulation strategy is proposed to further optimize phonon thermal transport across large-scale nanostructured interfaces.

4.1. Uniform interface roughness

The uniform roughness for horizontal and vertical interfaces is first considered at large-scale nanostructured interface by SKMC, with the physical model in Fig. 7. Al(1)/Si(2) and Ge(1)/Si(2) material pairs are considered with phonon dispersions and relaxation times consistent with before. The upper and lower boundary temperatures in y direction are set as $T_{\mathrm{H}} = 303$ K and $T_{\mathrm{C}} = 297$ K, respectively, and the boundaries along x and z directions are set as periodic boundary condition. The sizes of films are referred to the experiment in Ref. [50] for comparisons, taken as (87 nm+L_{c})× (87 nm+L_{c})× 1100 nm with pillar spacings L_{c} as 15, 57, 104 and 148 nm. The truncated cone interface in experiment is replaced by the cuboid interface with the same volume, whose size is derived as $L_{\mathrm{a}} \times L_{\mathrm{a}} \times L_{\mathrm{b}}$ with pillar width $L_{\mathrm{a}} = 65$ nm and heights L_{b} as 30, 50 and 64 nm. The roughnesses for the horizontal and vertical interfaces uniformly increase from 0.02 to 0.2 nm with the common difference 0.02 nm and from 0.2 to 1.8 nm with the common difference 0.2 nm, denoted by η_{h} and η_{v}, respectively. Particularly, for the case in present subsection with the uniform interface roughness, $\eta = \eta_{\mathrm{h}} = \eta_{\mathrm{v}}$. The total number of energy packets is set as 120,000,000 in all simulations. The

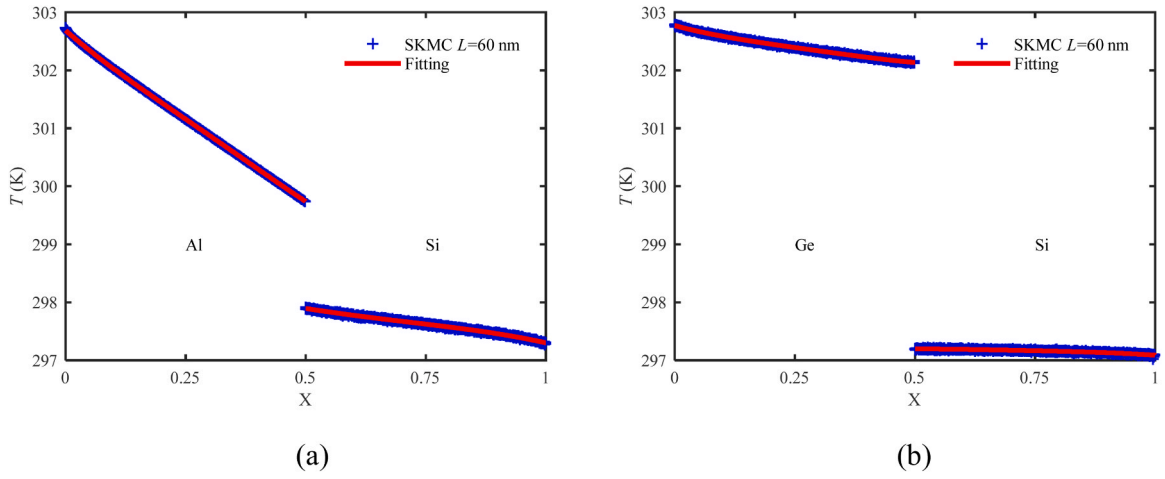


Fig. 3. Two fitting results for the steady-state temperature distribution of bilayer films: (a) Al/Si film and (b) Ge/Si film. The interface roughness and material ratio of film here are 0.15 nm and 1, respectively.

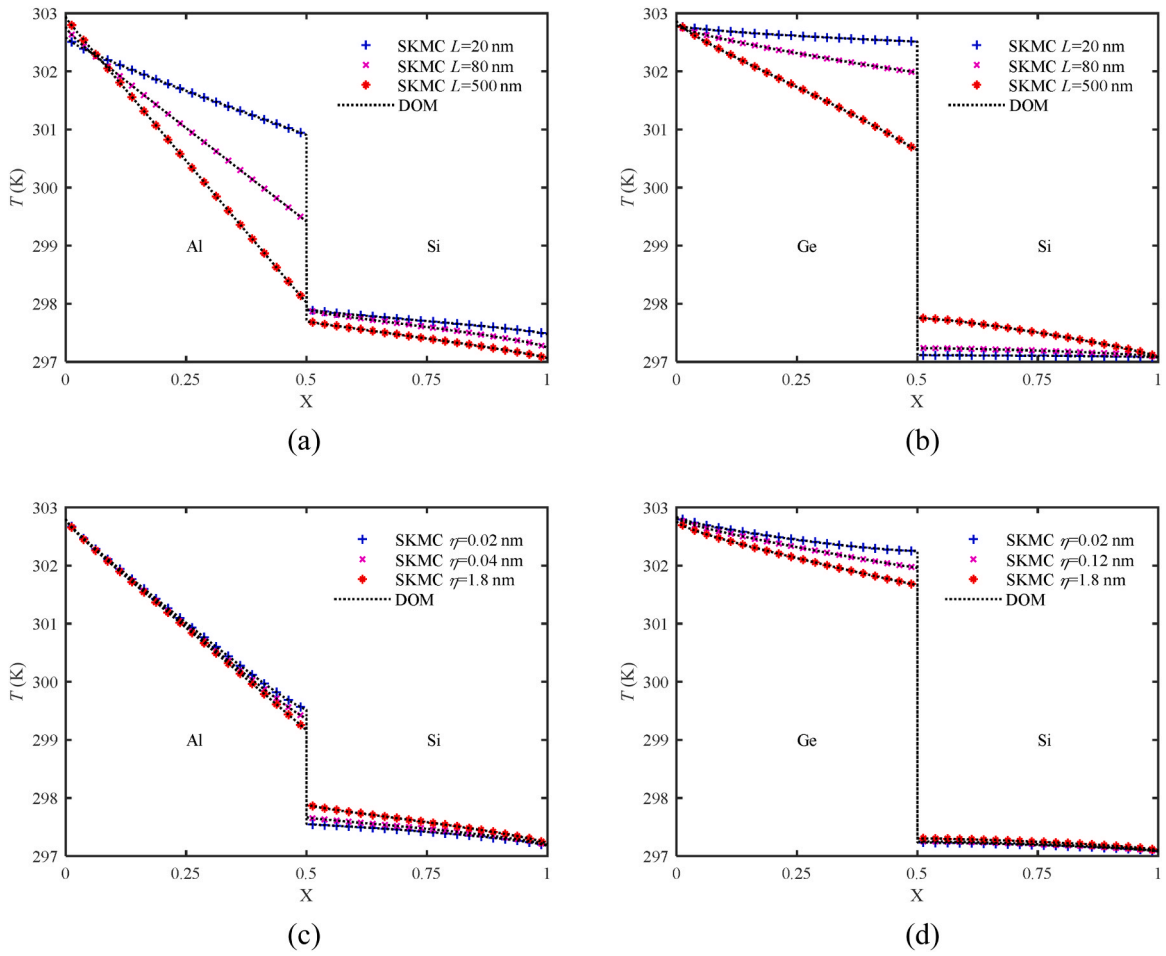


Fig. 4. The steady-state temperature distribution at various total thicknesses and interface roughnesses of bilayer films: (a) Al/Si film at various total thicknesses, (b) Ge/Si film at various total thicknesses, (c) Al/Si film at various interface roughnesses and (d) Ge/Si film at various interface roughnesses.

thermal conductivity is calculated by the formula based on Fourier's law, $\kappa = \left(L_y \int_0^{L_z} \int_0^{L_x} q_y \mathrm{d}x\mathrm{d}z\right)/(L_x L_z (T_\mathrm{H} - T_\mathrm{C}))$, with total thickness of film $L_y = 1100$ nm in y direction and size of film $L_x = L_z = (87\ \mathrm{nm} + L_\mathrm{c})$ in x and z directions. The thermal conductivity is adopted to investigate the impact of interface roughness on phonon thermal transport in present work.

In this subsection, the thermal conductivity is first compared between the simulation and experiment, and then studied at various uniform roughnesses of horizontal and vertical interfaces. To compare with experiment in Ref. [50], the thermal conductivity in experiment is calculated based on the one-dimensional thermal resistance model in Refs. [9,18,51]

$$\frac{L}{\kappa} = R_0 + \frac{1}{G}, \tag{10}$$

with the sum of thermal resistances R_0 excluding thermal boundary resistance, including boundary and intrinsic resistances and the thermal boundary conductance G. R_0 is $(L_\mathrm{Al}/\kappa_\mathrm{Al} + L_\mathrm{Si}/\kappa_\mathrm{Si})$ with thicknesses of Al and Si $L_\mathrm{Al} = 100$ nm and $L_\mathrm{Si} = 1000$ nm and bulk thermal conductivities of Al and Si, κ_Al and κ_Si. Due to only contribution from phonons is considered, κ_Al and κ_Si equal the lattice thermal conductivities of Al and Si, respectively, obtained based on phonon dispersions and relaxation times. G of the planar or nanostructured interface in experiment is calculated by averaging its original values with the error bars. The experiment adopted the bulk thermal conductivities of Al and Si to fit the measured temperature evolution to obtain the thermal boundary conductance, which approach is roughly consistent with the one-dimensional thermal resistance model in Eq. (10). Thus the measured thermal conductivity of bilayer film with nanostructured interfaces can be roughly obtained from Eq. (10) by applying the thermal boundary conductance in the experiment.

Fig. 8(a) and (b) show the thermal conductivities from SKMC and experiment in Ref. [50] at interface roughness being 0.3 nm and various pillar heights and spacings, providing qualitatively consistent varying trends and further validating the present MC. To better elucidate the impact of interface geometry on thermal conductivity, an effective interface area ratio is defined as

$$S_\mathrm{ratio} = \frac{L_x \cdot L_y + 4L_\mathrm{a} \cdot L_\mathrm{b}}{L_x \cdot L_y}. \tag{11}$$

The thermal conductivity is found to roughly increase with increasing effective interface area ratio in Fig. 8(c) and (d). The results indicate that large-scale nanostructured interface always facilitates interfacial phonon transport due to additional thermal conduction pathways by increasing interface area, consistent with previous conclusions [8,11–17]. In addition, Fig. 9 gives the thermal conductivities for six structures at various uniform horizontal and vertical interface roughnesses for Al/Si and Ge/Si, with those of planar interface at $L_\mathrm{Al} = 100$ nm and $L_\mathrm{Si} = 1000$ nm for comparison. To quantify the improvement by nanostructured interface, two improvement rates of thermal conductivity are defined as below

$$\gamma_1(\eta_{\mathrm{v,h}}) = \frac{\left|\kappa_\mathrm{nano}(\eta_{\mathrm{v,h}}) - \kappa_0(\eta_\mathrm{v})\right|}{\kappa_0(\eta_\mathrm{v})}, \tag{12}$$

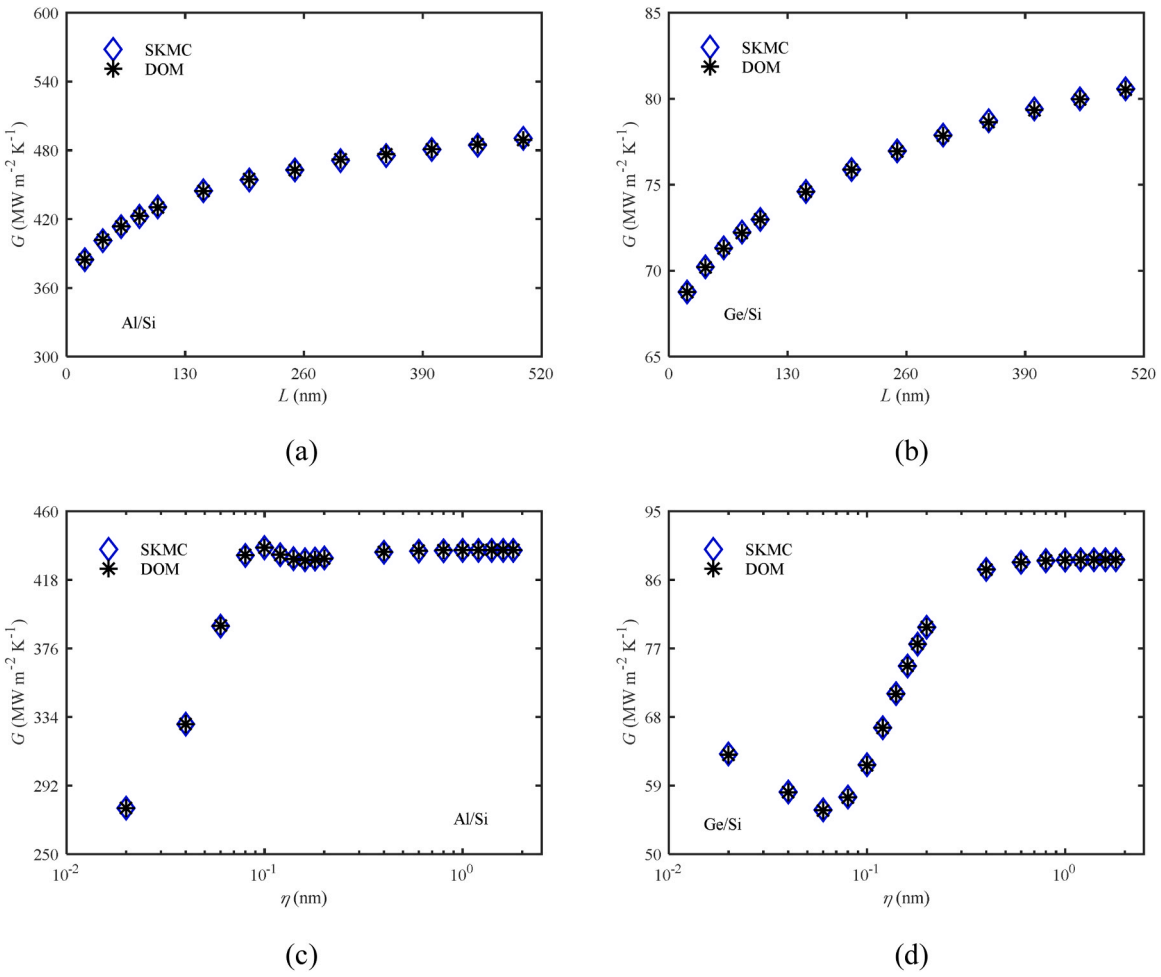


Fig. 5. The thermal boundary conductance at various total thicknesses and interface roughnesses of bilayer films: (a) Al/Si film at various total thicknesses, (b) Ge/Si film at various total thicknesses, (c) Al/Si film at various interface roughnesses and (d) Ge/Si film at various interface roughnesses.

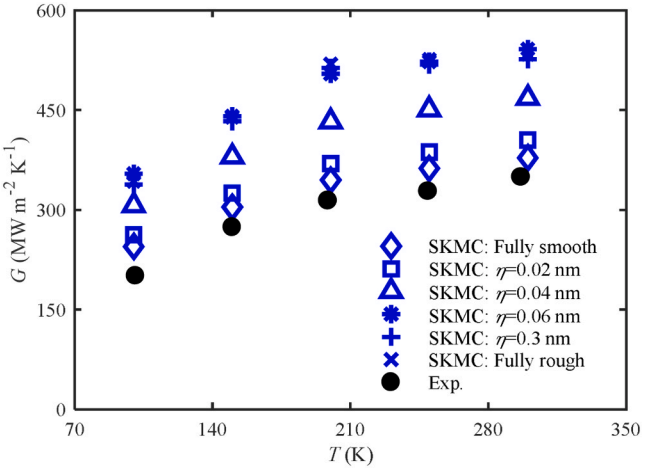


Fig. 6. The comparison of thermal boundary conductance between the present SKMC and experiment for Al/Si film at various temperatures. The abbreviation Exp. represents the result from experiment, referred to Refs. [47,48] here.

$$\gamma_2(\eta_{v,h}) = \frac{\left|\kappa_{nano}(\eta_{v,h}) - \kappa_0^{max}\right|}{\kappa_0^{max}}, \tag{13}$$

with κ_{nano} being the thermal conductivity for nanostructured interface at horizontal and vertical interface roughnesses being η_v and η_h, respectively, κ_0 being the thermal conductivity for planar interface at interface roughness being η_v, κ_0^{max} being the maximal thermal conductivity of planar interface throughout the entire roughness range, and γ_1 and γ_2 being the improvement rates compared with the planar interface at the same roughness as the vertical interface and the maximal thermal conductivity of planar interface throughout the entire roughness range, respectively. For Al/Si, the thermal conductivity first increases, and then

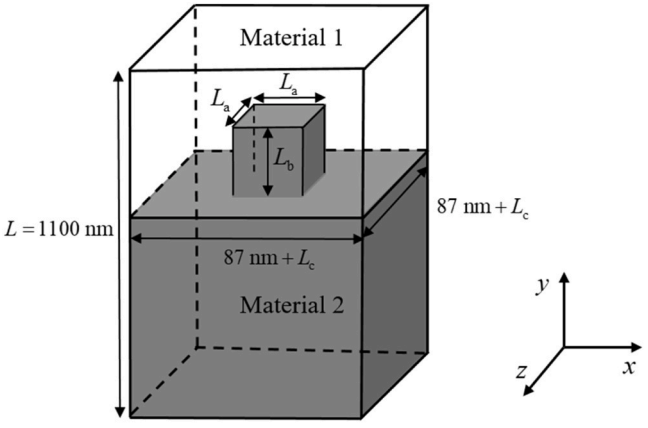


Fig. 7. Schematic diagram of bilayer film with large-scale nanostructured interface.

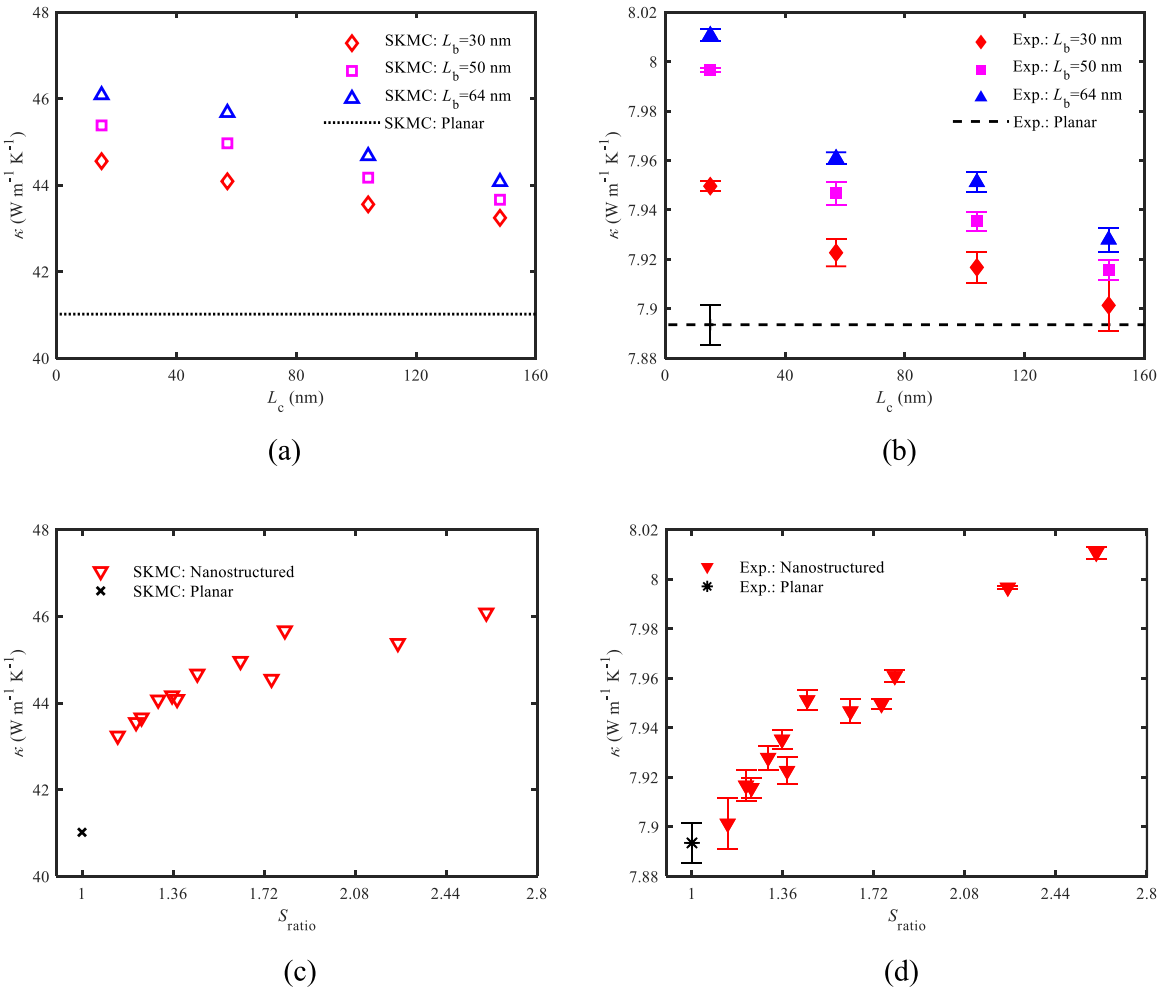


Fig. 8. The thermal conductivity of Al/Si bilayer film at various nanostructured interfaces by the present SKMC and experiment: (a) the thermal conductivity at various pillar heights and spacings by SKMC, (b) the thermal conductivity at various pillar heights and spacings by experiment, (c) the thermal conductivity at various effective interface area ratios by SKMC and (d) the thermal conductivity at various effective interface area ratios by experiment. The result by experiment is referred to Ref. [50] here.

decreases, and finally tends to remain unchanged for both large-scale nanostructured and planar interfaces. For all structures with changing horizontal and vertical interface roughnesses uniformly, the maximal and minimal γ_1 are 15.43% and 5.20%, respectively, and the maximal and minimal γ_2 are 15.18% and 1.32%, respectively. Whereas for Ge/Si, the thermal conductivity first increases, and then slightly decreases, and finally tends to remain unchanged for structures $L_c = 15$ nm and $L_b = 50$ nm, and $L_c = 15$ nm and $L_b = 64$ nm, and monotonically increases for the remaining structures, different from those for planar interface. For all structures with changing horizontal and vertical interface roughnesses uniformly, the maximal and minimal γ_1 are 53.59% and 9.81%, respectively, and the maximal and minimal γ_2 are 27.47% and −1.84% respectively. The above improvement rates indicate the interface roughness of nanostructured interface strongly impacts phonon thermal transport across large-scale nanostructured interfaces, resulting in either enhancement or suppression compared with planar interface.

Particularly, several issues need be clarified about the impacts of neglect of the electronic contribution, the inelastic scattering, the mode conversion, the phonon confinement and interfacial phonon modes revealed in Ref. [52]. First, although the neglect of the electronic contribution, inelastic scattering and mode conversion result in the underestimation of thermal conductivity [46], the semiquantitative variation of thermal conductivity with interface roughness and the corresponding manipulation still hold, which constitute the main focus of present work. Meanwhile, although there are quantitative differences, the conclusion with consistent semiquantitative trend between simulation and experiment in Fig. 8 remains valid. Secondly, with reducing characteristic dimensions, phonon dispersions and relaxation times increasingly deviate from the bulk properties, where the phonon confinement effect becomes increasingly important, especially below 10 nm. The thermal conductivity also increasingly deviates from the real situation when adopting the bulk phonon dispersions and relaxation times, as in present work. However, the dependence characteristic of thermal conductivity on the interface roughness is still valid. In addition, due to the nanostructured interfaces with characteristic dimensions on the order of bulk phonon mean free paths are considered, the impact of phonon confinement is mitigated. Thirdly, Ref. [52] has revealed that atomic vibrations near the interface can excite two distinct interfacial phonon modes, which enhance elastic scattering and dominate inelastic scattering at interface. Thus the present work may underestimate the thermal conductivity by neglecting these interfacial phonon modes. However, this limitation does not alter the core conclusion about the impact of interface roughness on thermal conductivity. And this underestimations for large-scale nanostructured interfaces is smaller than that for small-scale nanostructured interfaces. Finally, since the scenarios in subsections 4.2 and 4.3 are similar to this subsection, where the analyses for the above impacts are similar, further elaboration on these points will be omitted.

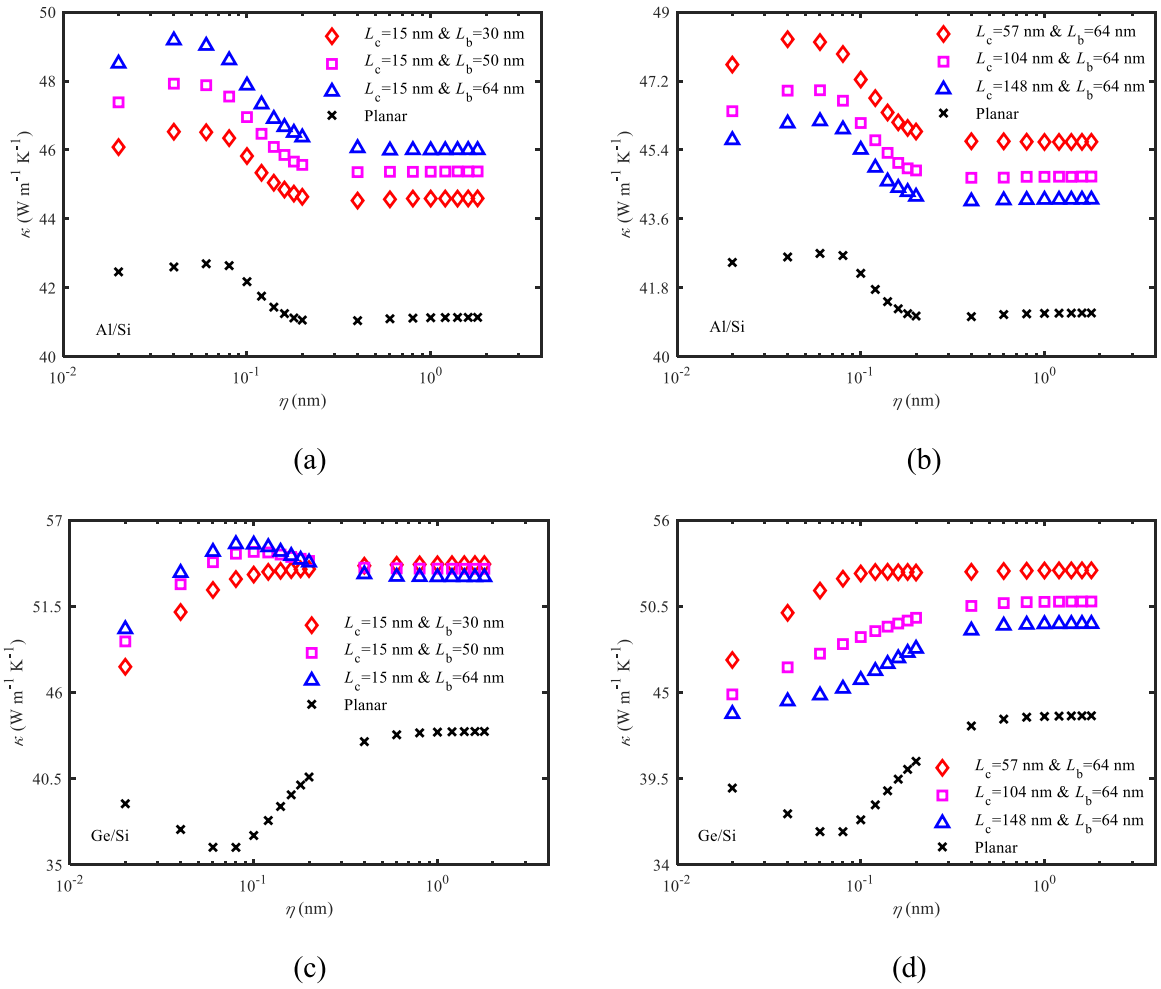


Fig. 9. The thermal conductivity of bilayer film at changing horizontal and vertical interface roughnesses uniformly: (a) Al/Si bilayer films with different pillar heights, (b) Al/Si bilayer films with different pillar spacings, (c) Ge/Si bilayer films with different pillar heights and (d) Ge/Si bilayer films with different pillar spacings.

4.2. Nonuniform interface roughness

The nonuniform roughness for horizontal and vertical interfaces is subsequently considered with physical model in Fig. 7. Two material pairs are considered, i.e. Al(1)/Si(2) and Ge(1)/Si(2), with the same phonon dispersions and relaxation times as before. The boundary condition, size of films, total number of energy packets, as well as the width, height and spacing of the pillars, are kept identical to those in Section 4.1. The nonuniform interface roughness contains two cases, i.e. fixing the horizontal interface roughness at 0.14 nm and increasing the vertical interface roughness from 0.02 to 0.2 nm with the common difference 0.02 nm and from 0.2 to 1.8 nm with the common difference 0.2 nm, and fixing the vertical interface roughness at 0.14 nm and increasing the horizontal interface roughness from 0.02 to 0.2 nm with the common difference 0.02 nm and from 0.2 to 1.8 nm with the common difference 0.2 nm. The thermal conductivity is calculated based on Fourier's law after obtaining the steady-state heat flux. In this subsection, the thermal conductivity is studied at various nonuniform roughnesses of horizontal and vertical interfaces.

Fig. 10 gives some of the results for thermal conductivity at various vertical interface roughnesses, including comparisons with planar interface at $L_{Al} = 100$ nm, $L_{Si} = 1000$ nm and the same roughness as the vertical interface. For Al/Si, the thermal conductivity first remains almost unchanged, and then decreases, and finally tends to remain unchanged for structures L_c being 15 nm and L_b being 30, 50 and 64 nm, and first slightly increases, and then decreases, and finally tends remain unchanged for the remaining structures, similar to planar interface. For all structures, the maximal and minimal γ_1 are 13.55% and 5.12%, respectively, and the maximal and minimal γ_2 are 12.18% and 1.46%, respectively. Whereas for Ge/Si, the thermal conductivity first decreases, and then increases, and finally tends to remain unchanged for all structures. The trend is similar to that for the planar interface with smaller changing magnitudes. For all structures, the maximal and minimal γ_1 are 55.03% and 12.39%, respectively, and the maximal and minimal γ_2 are 30.28% and 0.54%, respectively. The above results indicate the impact of vertical interface roughness on phonon thermal transport across large-scale nanostructured interfaces is similar to that of planar interface.

Fig. 11 gives some of the results for thermal conductivity at various horizontal interface roughnesses, including comparisons with planar interface at $L_{Al} = 100$ nm, $L_{Si} = 1000$ nm and the same roughness as the vertical interface. For Al/Si, the thermal conductivity first increases, and then slightly decreases, and finally tends to remain unchanged, similar to that with changing the vertical interface roughness solely. For all structures, the maximal and minimal γ_1 are 13.57% and 2.40%, respectively, and the maximal and minimal γ_2 are 12.19% and 2.06%, respectively. Whereas for Ge/Si, the thermal conductivity first dramatically increases, and then slightly decreases, and finally tends to remain unchanged, quite different from that with changing the vertical interface roughness solely. For all structures, the maximal and minimal γ_1 are 51.87% and 3.69%, respectively, and the maximal and minimal γ_2 are 26.61% and −2.43%, respectively. The above different improvement

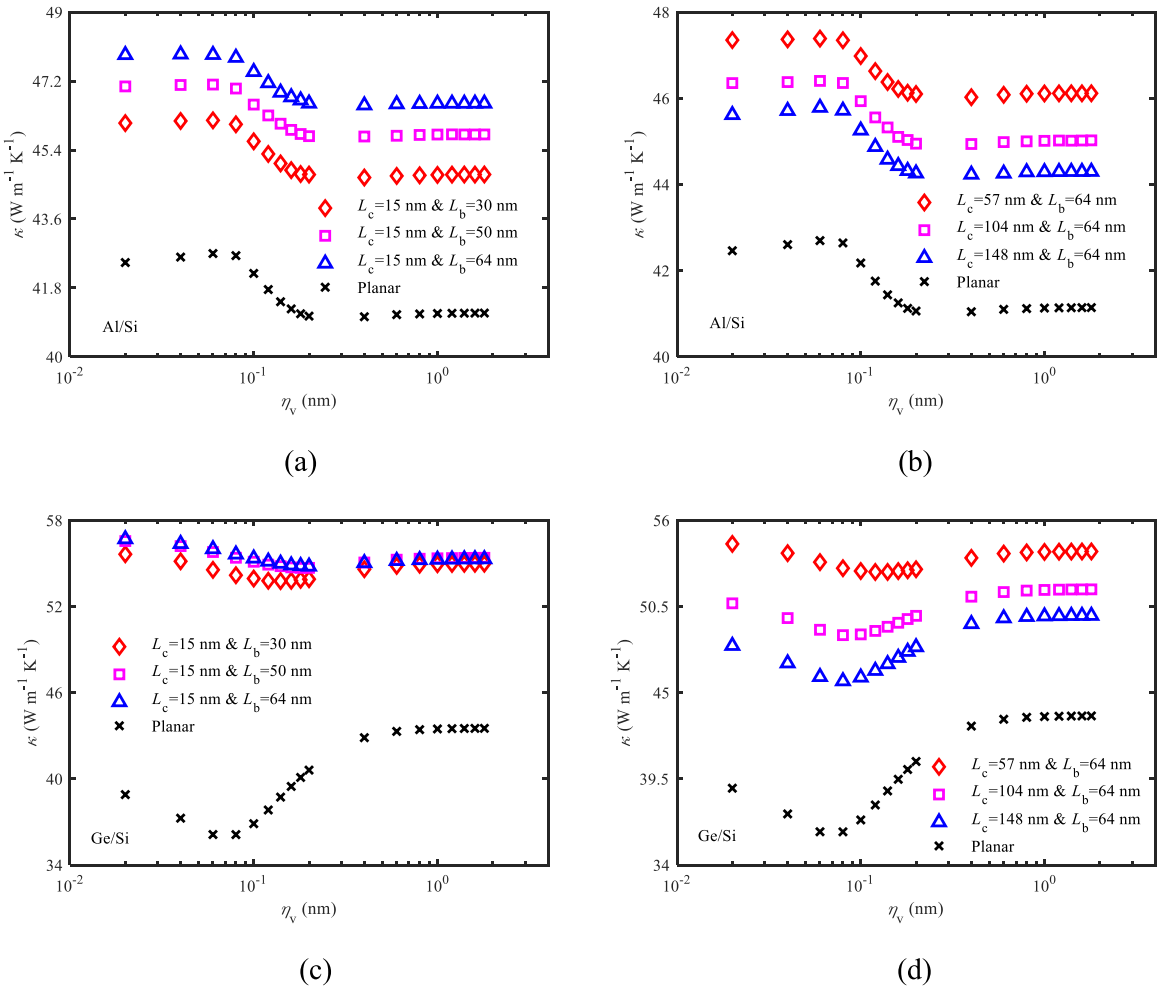


Fig. 10. The thermal conductivity of bilayer film at changing vertical and fixing horizontal interface roughnesses: (a) Al/Si bilayer films with different pillar heights, (b) Al/Si bilayer films with different pillar spacings, (c) Ge/Si bilayer films with different pillar heights and (d) Ge/Si bilayer films with different pillar spacings.

rates indicate a significant impact of interface roughness on phonon thermal transport across large-scale nanostructured interfaces, leading to either enhancement or suppression compared with planar interface. Moreover, it is suggested that such impact differs between horizontal and vertical interfaces as the interface roughness varies.

4.3. *Optimal interface roughnesses*

It is found that the thermal conductivity varies similarly with horizontal or vertical interface roughness for all structures. Thus in this subsection, the structure with pillar width L_a being 65 nm, spacing L_c being 15 nm and heights L_b being 64 nm is selected to study the optimal combination for maximizing thermal conductivity. The principle to select this structure as representative one is that its effective interface area ratio is largest, which can induce clearest optimization effect. Al (1)/Si(2) and Ge(1)/Si(2) with the same phonon dispersions and relaxation times as before are simulated, and the boundary condition, size of films and total number of energy packets are identical to those in Sections 4.1 and 4.2. The full matrix of roughness combination is encompassed for both horizontal and vertical interfaces. In detail, the horizontal interface roughness increases from 0.02 to 0.2 nm with the common difference 0.02 nm and from 0.2 to 1.8 nm with the common difference 0.2 nm, and the vertical interface roughness increases from 0.02 to 0.2 nm with the common difference 0.02 nm and from 0.2 to 1.8 nm with the common difference 0.2 nm, where there are a total of 324 cases. Then thermal conductivity is calculated with the steady-state heat flux based on Fourier's law.

In present subsection, only the thermal conductivity and improvement rate γ_2 are calculated and discussed at various roughness combinations in Fig. 12. For Al/Si, the thermal conductivity first remains almost unchanged or slightly increases, and then decreases, and finally tends to remain unchanged at each fixed horizontal interface roughness. And it first increases, and then slightly decreases, and finally tends to remain unchanged at each fixed vertical interface roughness. The optimal roughnesses for horizontal and vertical interfaces are obtained as 0.04 and 0.06 nm, respectively, with the maximal γ_2 being 15.21%. For Ge/Si, the thermal conductivity first decreases, and then increases, and finally tends to remain unchanged at each fixed horizontal interface roughness. And it first dramatically increases, and then slightly decreases, and finally tends to remain unchanged at each fixed vertical interface roughness. The optimal roughnesses for horizontal and vertical interfaces are obtained as 0.10 and 0.02 nm, respectively, with maximal γ_2 being 30.91%.

To further support the numerical robustness of the identified optimal roughnesses, the total number of energy packets is further set as 40,000,000, 80,000,000 and 160,000,000 whereas other numerical conditions are unchanged. For Al/Si, with a total packet number of 40,000,000 and 160,000,000, the optimal roughnesses remain 0.04 and 0.06 nm for the horizontal and vertical interfaces, respectively, identical to the total number of 120,000,000. With the total packet number of 80,000,000, these values are slightly adjusted to 0.04 nm and 0.02 nm, respectively. Moreover, the thermal conductivity with horizontal

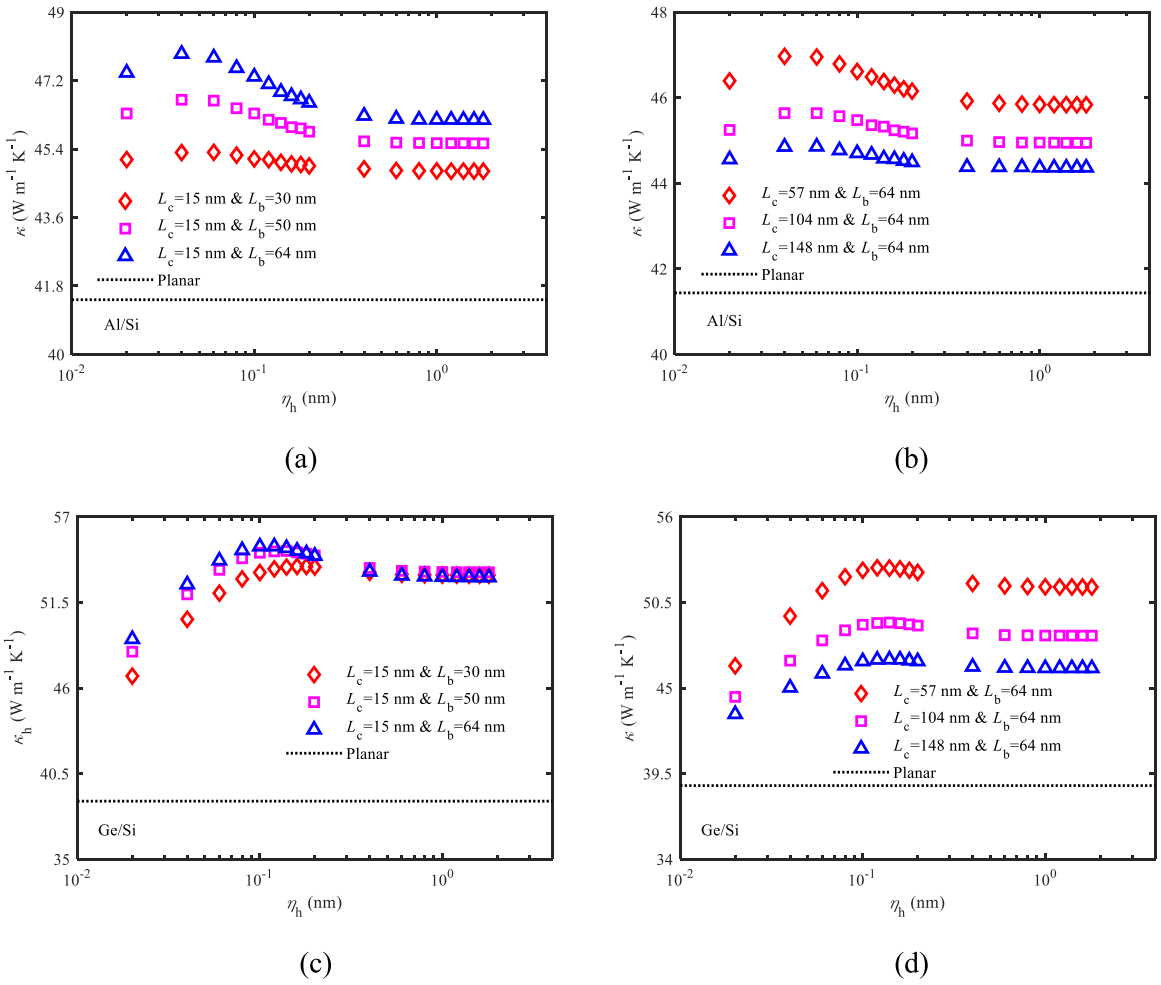


Fig. 11. The thermal conductivity of bilayer film at changing horizontal and fixing vertical interface roughnesses: (a) Al/Si bilayer films with different pillar heights, (b) Al/Si bilayer films with different pillar spacings, (c) Ge/Si bilayer films with different pillar heights and (d) Ge/Si bilayer films with different pillar spacings.

interface roughness being 0.04 nm and vertical interface roughness being 0.02 nm is 49.1925, 49.1972, 49.1854 and 49.1707 (W m^{-1} K^{-1}) for total packet numbers being 40,000,000, 80,000,000, 120,000,000 and 160,000,000, respectively. The thermal conductivity with horizontal interface roughness being 0.04 nm and vertical interface roughness being 0.06 nm is 49.2107, 49.1876, 49.1905 and 49.1826 (W m^{-1} K^{-1}) for above packet numbers, respectively. For Ge/Si, the optimal roughnesses for the horizontal and vertical interfaces are 0.10 nm and 0.02 nm, respectively, for all total packet numbers. And the thermal conductivity with horizontal interface roughness being 0.10 nm and vertical interface roughness being 0.02 nm is 56.9854, 56.9862, 56.9680 and 56.9746 (W m^{-1} K^{-1}) for above packet numbers, respectively. The results provide the virtually unchanged thermal conductivity with increasing total packet number, supporting the numerical robustness for thermal conductivity calculation. For the identified optimal roughness combination, the conclusion is consistent in all cases except for the case with the total packet number being 80,000,000 in Al/Si. For this special case, a distinct optimal roughness combination is obtained; specifically, the optimal roughness for horizontal interface is consistent with other cases, whereas that for vertical interface exhibits a slight deviation. However, accounting for the noise error in Monte Carlo simulation, this slight deviation for the vertical interface is acceptable, as the thermal conductivities with the two roughness combinations remain remarkably close across four total packet numbers. It is worth noting that, since only one representative structure is selected to do the optimization here, the obtained optimal horizontal and vertical interface roughnesses are not universal for all structures. However, the optimal interface roughnesses are inferred to be close to the obtained optimal interface roughnesses due to the thermal conductivity of all structures varies with interface roughnesses similarly.

In present work, four factors are introduced to explain the above varying trends and corresponding optimal interface roughness combinations, including interface transmissivity, interfacial scattering mechanism, additional thermal conduction pathway and multiple coupled interfacial scattering events. For one material pair, the interface roughness directly influences the interface transmissivity and interfacial scattering mechanism. The nanostructured interface increases the contact area between two materials, subsequently resulting in additional thermal conduction pathway, and also introduces multiple coupled interfacial scattering events. First, for the interface transmissivity, the varying interface roughness leads to the varying overall interface transmissivity [33], hence changing the thermal boundary conductance, which is mainly associated with the vertical interface. Considering this factor in isolation, a larger thermal boundary conductance at vertical interfaces leads to a larger thermal conductivity for nanostructured interface. Secondly, for interfacial scattering mechanism, a phonon is more likely to be specularly scattered by interface at low interface roughness and diffusely scattered by interface at large interface roughness, affecting interfacial phonon transport. The effect of this factor is mainly associated with horizontal interfaces, providing an increased extra thermal resistance in heat flux direction with increasing horizontal interface roughness. This is due to the specular scattering at interfaces poses no thermal resistance whereas the diffuse scattering at interfaces induces thermal resistance through resistive scattering in heat flux

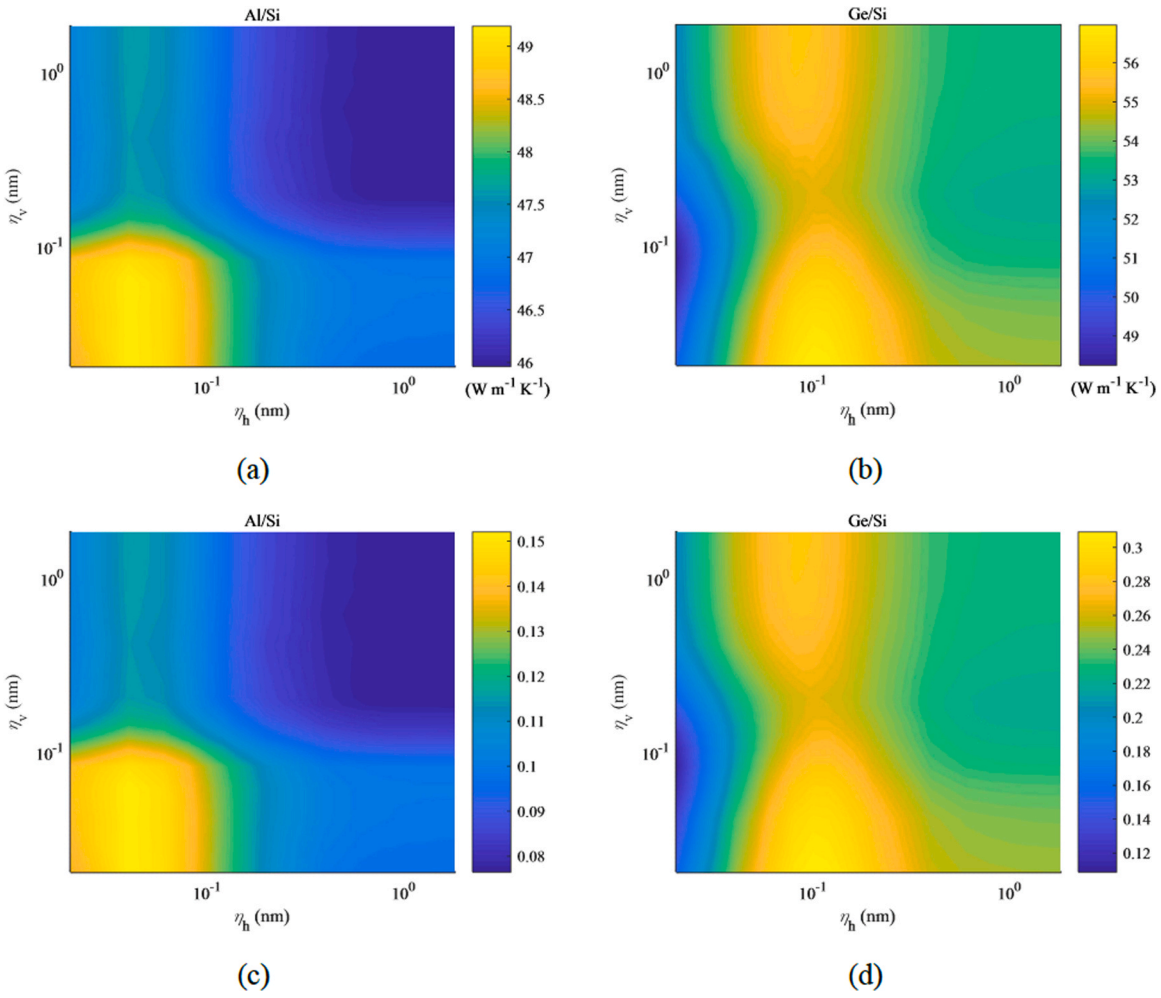


Fig. 12. The thermal conductivity and improvement rate of bilayer film with nanostructured interface at various roughness combinations: (a) thermal conductivity of Al/Si film, (b) thermal conductivity of Ge/Si film, (c) improvement rate for Al/Si film and (d) improvement rate for Ge/Si film. The nanostructured interface features pillar height of 64 nm and spacing of 15 nm. The improvement rate is obtained by comparing thermal conductivity for nanostructured interface with the maximal thermal conductivity of planar interface throughout the entire roughness range.

direction. This factor has been explained in previous works in detail [18,53]. Thirdly, the additional thermal conduction pathway induced by increasing contact area through nanostructured interfaces can facilitate interfacial phonon transport, similar to the macroscale fin arrays facilitating heat transfer between solid surfaces and fluids, revealed in previous works [13,15,16,50]. Finally, multiple coupled interfacial scattering events will occur at nanostructured interface for individual phonons, and the frequency of events is higher at large-scale nanostructured interface than at small-scale counterparts due to larger size. These scattering events are correlated and collectively influence the detailed interfacial scattering processes, hence affecting interfacial phonon transport. This factor has been introduced to explain the difference of phonon thermal transport across the fully smooth and the fully rough nanostructured interfaces before, yet lacking detailed analyses [54].

Based on the above introduction, the roughness impact of the vertical and horizontal interfaces are elucidated at large-scale nanostructured interface below. When changing vertical interface roughness, phonon transport across nanostructured interface is mainly affected by the change of vertical interface. Thus, the thermal conductivity with nanostructured interfaces exhibits a similar trend to the variation of thermal boundary conductance of planar interface with interface roughness, associated with the interface transmissivity. For Al/Si, the thermal boundary conductance of planar interface first increases, and then decreases, and finally tends to remain unchanged with increasing interface roughness. Hence the thermal conductivity of films with nanostructured interface first increases, and then slightly decreases, and finally tends to remain unchanged. For Ge/Si, the thermal boundary conductance of planar interface first decreases, and then increases, and finally tends to remain unchanged with increasing interface roughness. Hence the thermal conductivity of films with nanostructured interface first decreases, and then increases, and finally tends to remain unchanged. Additionally, multiple coupled interfacial scattering events at nanostructured interfaces can make the varying trend of thermal conductivity with interface roughness deviate from that of thermal boundary conductance of planar interface for both material pairs. To explain this deviation, the vertical interface is further divided into two categories, including interfaces near the heat sink and heat source. On the one hand, reflected phonons by vertical interface near the heat sink can be secondarily scattered by horizontal interface, redirecting their moving directions. Consequently, these phonons have a high probability of moving forward again and transmitting across this vertical interface toward the heat sink, resulting in the increase of thermal conductivity, illustrated in Fig. 13 (b). Thus, although a certain thermal boundary conductance of planar interface is not maximal, the thermal conductivity with corresponding vertical interfaces can still reach the maximum. On the other hand, the maximal thermal boundary conductance of planar interface is associated with maximal overall interface

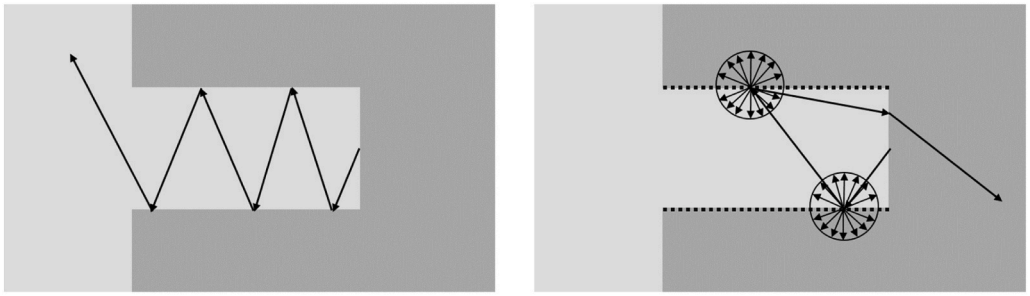


Fig. 13. The illustration for the multiple coupled interfacial scattering events at large-scale nanostructured interface: (a) low-roughness horizontal interface and (b) high-roughness horizontal interface. Dotted lines in (b) represent the horizontal interfaces are rough. The heat flux direction is from the left to right side.

transmissivity at corresponding vertical interfaces. Backward phonons scattered by such vertical interface near the heat source exhibit a high probability of transmitting the interface and moving toward the heat source, resulting in the reduction of thermal conductivity. Therefore, an interface roughness to induce near-maximal thermal boundary conductance is recommended for the vertical interface of large-scale nanostructured interfaces.

When changing the horizontal interface roughness, phonon transport across nanostructured interface is mainly affected by the change of horizontal interface. The extra thermal resistance induced by resistive scattering at horizontal interfaces increases with increasing roughness considering single interfacial scattering. Nevertheless, each phonon can undergo multiple coupled interfacial scattering events at nanostructured interfaces, which strongly impacts the probability of one phonon transmitting the interface, illustrated in Fig. 13. In detail, at low horizontal interface roughness, backward phonons are more likely specularly scattered at horizontal interface and unlikely to redirect their trajectory to move along the heat flux, resulting in the reduction of thermal conductivity. Whereas at high horizontal interface roughness, backward phonons are more likely diffusely scattered at horizontal interface to redirect their trajectories to move along the heat flux, resulting in the increase of thermal conductivity. Therefore, an interface roughness to induce partially specular and partially diffuse interfacial scattering and prevent excessive resistive scattering is recommended for the horizontal interface of large-scale nanostructured interfaces.

Furthermore, the differential impacts of interface roughness on thermal conductivity are examined between large-scale nanostructured interfaces and other structures. On the one hand, the varying trend of thermal conductivity with horizontal and vertical interface roughnesses for large-scale nanostructured interfaces differs from that for small-scale nanostructured interfaces in Ref. [18]. For large-scale nanostructured interface, the maximal thermal conductivity is achieved at vertical interface roughness corresponding to near-maximal thermal boundary conductance of planar interface, and at horizontal interface that is partially rough and partially smooth. Whereas for small-scale nanostructured interface, the maximal thermal conductivity is achieved at vertical interface roughness corresponding to the maximal thermal boundary conductance of planar interface, and at fully smooth horizontal interface. The detailed reason is analyzed as follow: At nanostructured interfaces, a single phonon is scattered multiple times that are correlated; the coupled interfacial scattering times of one phonon at large-scale nanostructured interfaces are much more than that at small-scale nanostructured interfaces, making the effect of multiple coupled interfacial scattering events at the former interface stronger; thus at large-scale nanostructured interfaces, interface transmissivity, interfacial scattering mechanism, additional thermal conduction pathway and multiple coupled interfacial scattering events synergistically impact interfacial phonon transport, resulting in the above varying trend; whereas at small-scale nanostructured interfaces, single interfacial scattering dominates, making interface transmissivity and interfacial scattering mechanism the dominant impact factors and additional thermal conduction pathway the secondary impact factor; the effects of the former two are mainly reflected by the vertical and horizontal interface roughnesses, respectively, with results introduced before. On the other hand, due to the characteristic size on the order of phonon mean free paths, interfacial scattering at large-scale nanostructured interfaces is different from that at the macroscale. The interface roughness serves as the critical factor to impact detailed interfacial scattering processes, which govern thermal transport across nanostructured interfaces. In contrast, at the macroscale, the additional thermal conduction pathway dominates thermal transport and is mainly determined by contact area or interface geometry, while the other three factors can be neglected due to intrinsic scattering prevails over interfacial scattering.

Totally, based on the analyses above, the semiquantitative strategy to select the optimal interface roughness to maximize thermal conductivity is as follow: The vertical interface roughness is selected to obtain a near-maximal thermal boundary conductance for planar interface, which not only ensures sufficiently large forward transmitting probability along the heat flux but also prevents excessively large backward transmitting probability in the opposite direction of heat flux; the horizontal interface is selected to be partially rough and partially smooth, and this design can not only prevent overly large extra thermal resistance by resistive scattering but also leverages multiple coupled interfacial scattering events to redirect the trajectories of backward phonons to move along the heat flux. Moreover, at partially rough and partially smooth horizontal interfaces, the secondary reflection can mitigate the adverse impact on enhancing thermal conductivity caused by non-maximal overall interface transmissivity at vertical interfaces, which corresponds to the near-maximal thermal boundary conductance of planar interface.

5. Conclusions

In summary, the present work reports a significant impact of interface roughness on phonon transport across large-scale nanostructured interfaces with characteristic size on the order of phonon mean free paths, and develops a semiquantitative strategy to further optimize interfacial phonon transport via tailoring interface roughness. Twelve structures are first simulated to study the interface roughness impact and one of them is then selected to determine the optimal interface roughness combination to maxmize thermal conductivity. The results show similar manipulation trends of thermal conductivity at Al/Si large-scale nanostructured interfaces when varying the vertical and horizontal interface roughnesses uniformly and nonuniformly, resembling those of planar interfaces. In contrast, Ge/Si large-scale nanostructured interfaces display the divergent manipulation behaviors notably from each other and from those of planar interfaces under the same conditions. In

addition, when compared with the planar interface at the same roughness as the vertical interface, interfacial phonon transport is always facilitated with different optimization effects at different interface roughnesses. Yet it can be either facilitated or suppressed by large-scale nanostructured interface when compared with the maximal thermal conductivity of planar interface throughout the entire roughness range. Thus it is critical to reasonably tailor interface roughness for the facilitation through large-scale nanostructured interfaces; otherwise, facilitation is unattainable.

In detail, when changing the horizontal and vertical interface roughnesses uniformly, the thermal conductivity of bilayer film first increases, and then decreases, and finally tends to remain unchanged for Al/Si. And it first increases, and then slightly decreases, and finally tends to remain unchanged for Ge/Si. When changing the vertical and fixing the horizontal interface roughnesses, the thermal conductivity of bilayer film first remains almost unchanged or slightly increases, and then decreases, and finally tends to remain unchanged for Al/Si. And it first decreases, and then increases, and finally tends to remain unchanged for Ge/Si. When changing the horizontal and fixing the vertical interface roughnesses, the thermal conductivity of bilayer film first increases, and then slightly decreases, and finally tends to remain unchanged for Al/Si. And it first dramatically increases, and then slightly decreases, and finally tends to remain unchanged for Ge/Si. Among all cases, the maximal and minimal improvement rates of thermal conductivity are 15.43% and 2.40% for Al/Si, and 55.03% and 3.69% for Ge/Si, respectively, compared to the planar interface at the same roughness as the vertical interface. And they are 15.18% and 1.31% for Al/Si, and 30.28% and −2.43% for Ge/Si, respectively, compared to the maximal thermal conductivity of planar interface throughout the entire roughness range.

Since the thermal conductivity varies with horizontal and vertical interface roughnesses similarly for current large-scale nanostructured interfaces, the maximal thermal conductivity of all structures is inferred to be achieved under similar interface roughness combinations. Thereby, without loss of generality, one structure is simulated throughout full matrix of roughness combination to identify the optimal interface roughness combination for maximizing thermal conductivity. Such optimal roughness combinations for horizontal and vertical interfaces of this representative structure are 0.04 nm and 0.06 nm for Al/Si, and 0.10 nm and 0.02 nm for Ge/Si, respectively. And the corresponding improvement rates are 15.21% and 30.91% for Al/Si and Ge/Si, respectively, compared with the maximal thermal conductivity of planar interface throughout the entire roughness range. It should be noted that the optimal roughness combinations of other structures may deviate from the above slightly. The present work attributes above results to the combined effect induced by large-scale nanostructured interfaces, involving transmission probability, extra thermal resistance in heat flux direction, contact area and phonon trajectory redirection. These phenomena are governed by interface transmissivity, interfacial scattering mechanism, additional thermal conduction pathway and multiple coupled interfacial scattering events, respectively. Based on this effect, a specific interface roughness is recommended for the vertical interface to achieve a near-maximal thermal boundary conductance for planar interface, whereas the horizontal interface is recommended to be partially rough and partially smooth. It is demonstrated that phonon thermal transport across large-scale nanostructured interfaces can be further optimized with this semiquantitative strategy. The current results emphasize the importance of tailoring interface roughness on the manipulation of thermal conductivity through large-scale nanostructured interface, and suggest that the manipulation can be further optimized via tailoring interface roughness precisely.

CRediT authorship contribution statement

Xin Ran: Writing – original draft, Visualization, Methodology, Investigation, Funding acquisition, Formal analysis, Data curation, Conceptualization. **Bingyang Cao:** Writing – review & editing, Validation, Supervision, Project administration.

Declaration of Competing Interest

The authors declare that they have no known competing financial interests or personal relationships that could have appeared to influence the work reported in this paper.

Acknowledgements

This study was financially supported by the National Natural Science Foundation of China (No. 52425601), the Natural Science Foundation of Jiangsu Province (No. BK20250632), and the Natural Science Foundation for Colleges and Universities in Jiangsu Province (No. 25KJB140008).

References

[1] Y.-C. Hua, Y. Shen, Z.-L. Tang, D.-S. Tang, X. Ran, B.-Y. Cao, Near-junction thermal managements of electronics. in: Advances in Heat Transfer, Elsevier, Amsterdam, 2023, pp. 355–434.
[2] H. Wu, C. Yan, P. Chen, S. Wu, X. Gong, B. Zhang, G. Wang, H. Zou, Y. Yan, G. Ding, J. Liu, G. Han, G. Wang, X. Lu, D. Li, X. Zhou, Achieving superior thermoelectric performance in N-type SnS-based polycrystals by regulating donor dopability and phonon propagation, Acta Mater. 301 (2025) 121566.
[3] J. Chen, X. Xu, J. Zhou, B. Li, Interfacial thermal resistance: past, present, and future, Rev. Mod. Phys. 94 (2) (2022) 025002.
[4] D. Ma, Y. Zhao, L. Zhang, Facilitating thermal transport across Si/Ge interface via mass-graded interlayer: The role of elastic and inelastic phonon processes, J. Appl. Phys. 129 (17) (2021) 175302.
[5] I. Al Keyyam, X. Wang, Generalization of interfacial thermal conductance based on interfacial phonon localization, Mater. Today Phys. 46 (2024) 101516.
[6] B.-Y. Cao, Non-Fourier Heat Conduction in Nanostrucutres, Science Press, Beijing, 2023.
[7] G. Chen, Non-Fourier phonon heat conduction at the microscale and nanoscale, Nat. Rev. Phys. 3 (8) (2021) 555–569.
[8] M. Hu, X. Zhang, D. Poulikakos, C.P. Grigoropoulos, Large “near junction” thermal resistance reduction in electronics by interface nanoengineering, Int. J. Heat. Mass. Transf. 54 (25-26) (2011) 5183–5191.
[9] X. Ran, Y. Guo, M. Wang, Interfacial phonon transport with frequency-dependent transmissivity by Monte Carlo simulation, Int. J. Heat. Mass. Transf. 123 (2018) 616–628.
[10] P.E. Hopkins, L.M. Phinney, J.R. Serrano, T.E. Beechem, Effects of surface roughness and oxide layer on the thermal boundary conductance at aluminum/silicon interfaces, Phys. Rev. B 82 (8) (2010) 085307.
[11] X.W. Zhou, R.E. Jones, C.J. Kimmer, J.C. Duda, P.E. Hopkins, Relationship of thermal boundary conductance to structure from an analytical model plus molecular dynamics simulations, Phys. Rev. B 87 (9) (2013) 094303.
[12] E. Lee, T. Zhang, M. Hu, T. Luo, Thermal boundary conductance enhancement using experimentally achievable nanostructured interfaces–analytical study combined with molecular dynamics simulation, Phys. Chem. Chem. Phys. 18 (25) (2016) 16794–16801.
[13] E. Yin, Q. Li, W. Lian, Mechanisms for enhancing interfacial phonon thermal transport by large-size nanostructures, Phys. Chem. Chem. Phys. 25 (5) (2023) 3629–3638.
[14] W. Luo, N. Wang, W. Lian, E. Yin, Q. Li, Enhancing interfacial thermal transport by nanostructures: Monte Carlo simulations with ab initio phonon properties, J. Appl. Phys. 137 (6) (2025) 065102.
[15] W. Park, A. Sood, J. Park, M. Asheghi, R. Sinclair, K.E. Goodson, Enhanced thermal conduction through nanostructured interfaces, Nanoscale Microsc. Thermophys. Eng. 21 (3) (2017) 134–144.
[16] Y. Xu, G. Wang, Y. Zhou, Broadly manipulating the interfacial thermal energy transport across the Si/4H-SiC interfaces via nanopatterns, Int. J. Heat. Mass. Transf. 187 (2022) 122499.
[17] X. Zhao, X. Qian, X. Li, R. Yang, Thermal conductance of nanostructured interfaces from Monte Carlo simulations with ab initio-based phonon properties, J. Appl. Phys. 129 (21) (2021) 215105.
[18] X. Ran, B. Cao, Roughness dependence of phonon-interface thermal transport: theoretical model and Monte Carlo simulation, Phys. Rev. B 110 (2) (2024) 024302.
[19] W. Little, The transport of heat between dissimilar solids at low temperatures, Can. J. Phys. 37 (3) (1959) 334–349.
[20] E.T. Swartz, R.O. Pohl, Thermal boundary resistance, Rev. Mod. Phys. 61 (3) (1989) 605–668.
[21] G. Chen, Thermal conductivity and ballistic-phonon transport in the cross-plane direction of superlattices, Phys. Rev. B 57 (23) (1998) 14958.
[22] X. Li, R. Yang, Effect of lattice mismatch on phonon transmission and interface thermal conductance across dissimilar material interfaces, Phys. Rev. B 86 (5) (2012) 054305.

[23] C. Hua, X. Chen, N.K. Ravichandran, A.J. Minnich, Experimental metrology to obtain thermal phonon transmission coefficients at solid interfaces, Phys. Rev. B 95 (20) (2017) 205423.
[24] B. Liu, V.I. Khvesyuk, Analytical model for thermal boundary conductance based on elastic wave theory, Int. J. Heat. Mass. Transf. 159 (2020) 120117.
[25] J.-Y. Lin, M.-J. Huang, An investigation into the roughness and film thickness effects on the interfacial thermal resistance, Nanoscale Microsc. Thermophys. Eng. 27 (3-4) (2023) 149–167.
[26] J.C. Duda, P.E. Hopkins, J.L. Smoyer, M.L. Bauer, T.S. English, C.B. Saltonstall, P. M. Norris, On the assumption of detailed balance in prediction of diffusive transmission probability during interfacial transport, Nanoscale Microsc. Thermophys. Eng. 14 (1) (2010) 21–33.
[27] Y. Zhang, D. Ma, Y. Zang, X. Wang, N. Yang, A modified theoretical model to accurately account for interfacial roughness in predicting the interfacial thermal conductance, Front. Energy Res. 6 (2018) 48.
[28] M. Zhang, X. Huang, Y. Wang, C. Zhang, Y. Ni, Interfacial thermal conductance of functionalized graphene/fluoropolymer nanocomposites: synergistic interfacial effects on phonon transport, Int. J. Heat. Mass. Transf. 269 (2026) 129156.
[29] Z. Zong, S. Deng, Y. Qin, X. Wan, J. Zhan, D. Ma, N. Yang, Enhancing the interfacial thermal conductance of Si/PVDF by strengthening atomic couplings, Nanoscale 15 (40) (2023) 16472–16479.
[30] H. Huang, K. Yang, S. Hu, B. Zhong, Y. Wang, Q. Zhang, J. Ni, Y. Liu, X. Gu, Y. Liu, T. Fan, Significantly enhanced heat transport capability across nitrogen-doped graphene/metal interface through lattice substitution induced inelastic phonon scattering, Acta Mater. 306 (2026) 121908.
[31] S. Wang, D. Xu, R. Gurunathan, G.J. Snyder, Q. Hao, Thermal studies of individual Si/Ge heterojunctions — The influence of the alloy layer on the heterojunction, J. Mater. 6 (2) (2020) 248–255.
[32] J.-P.M. Peraud, C.D. Landon, N.G. Hadjiconstantinou, Monte Carlo methods for solving the Boltzmann transport equation, Annu. Rev. Heat. Transf. 17 (2014) 205–265.
[33] X. Ran, B. Cao, Roughness dependence of cross-plane interfacial phonon transport in multilayer films by discrete ordinates method, Mater. Today Chem. 49 (2025) 103023.
[34] M.-S. Jeng, R. Yang, D. Song, G. Chen, Modeling the thermal conductivity and phonon transport in nanoparticle composites using Monte Carlo simulation, J. Heat. Transf. 130 (2008) 042410.
[35] M.-J. Huang, T.-C. Tsai, L. Liang-Chun, M.-s Jeng, Y. Chang-Chung, A fast Monte-Carlo solver for phonon transport in nanostructured semiconductors, Comput. Model. Eng. & Sci. 42 (2) (2009) 107.
[36] T. Hori, J. Shiomi, C. Dames, Effective phonon mean free path in polycrystalline nanostructures, Appl. Phys. Lett. 106 (17) (2015) 171901.
[37] J. Yu, W. Ye, B. Huang, D.J. Villaroman, Q. Wang, MFP-based Monte Carlo method for nanostructure phonon transport, in: International Conference on Micro/Nanoscale Heat Transfer, American Society of Mechanical Engineers, Dalian, China, 2019. V001T010A006.
[38] X. Ran, M. Wang, In-plane interfacial phonon transport through multi-layer thin films by theoretical analyses and Monte Carlo simulations, Int. J. Heat. Mass. Transf. 176 (2021) 121438.
[39] Ge - Germanium, available from: http://www.ioffe.ru/SVA/NSM/Semicond/Ge/mechanic.html (Accessed accessed 1 January 2021 2021).
[40] Si - Silicon, available from: http://www.ioffe.ru/SVA/NSM/Semicond/Si/mechanic.html (Accessed accessed 1 January 2021 2021).
[41] Rt Stedman, G. Nilsson, Dispersion relations for phonons in aluminum at 80 and 300 K, Phys. Rev. 145 (2) (1966) 492–500.
[42] J.-P.M. Péraud, N.G. Hadjiconstantinou, Extending the range of validity of Fourier's law into the kinetic transport regime via asymptotic solution of the phonon Boltzmann transport equation, Phys. Rev. B 93 (4) (2016) 045424.
[43] A. Jain, A.J. McGaughey, Thermal transport by phonons and electrons in aluminum, silver, and gold from first principles, Phys. Rev. B 93 (8) (2016) 081206.
[44] B.S. Yilbas, S.B. Mansoor, Phonon transport and equivalent equilibrium temperature in thin silicon films, J. Non-Equilib. Thermodyn. 38 (2) (2013) 153–174.
[45] X. Ran, M. Wang, Efficiency improvement of discrete-ordinates method for interfacial phonon transport by Gauss-Legendre integral for frequency domain, J. Comput. Phys. 399 (2019) 108920.
[46] M.D.S. Féliciano, C. Adessi, J.E. Hajj, N. Horny, F. Detcheverry, M. Cobian, S. Merabia, First-principles calculations of thermal transport at metal/silicon interfaces: evidence of interfacial electron-phonon coupling, Phys. Rev. B 112 (24) (2025) 245303.
[47] C. Monachon, L. Weber, C. Dames, Thermal boundary conductance: a materials science perspective, Annu. Rev. Mater. Res. 46 (1) (2016) 433–463.
[48] A.J. Minnich, J.A. Johnson, A.J. Schmidt, K. Esfarjani, M.S. Dresselhaus, K. A. Nelson, G. Chen, Thermal conductivity spectroscopy technique to measure phonon mean free paths, Phys. Rev. Lett. 107 (9) (2011) 095901.
[49] P. Jiang, L. Lindsay, X. Huang, Y.K. Koh, Interfacial phonon scattering and transmission loss in> 1 μm thick silicon-on-insulator thin films, Phys. Rev. B 97 (19) (2018) 195308.
[50] E. Lee, T. Zhang, T. Yoo, Z. Guo, T. Luo, Nanostructures significantly enhance thermal transport across solid interfaces, ACS Appl. Mater. & Interfaces 8 (51) (2016) 35505–35512.
[51] P.E. Hopkins, J.R. Serrano, L.M. Phinney, S.P. Kearney, T.W. Grasser, C. Thomas Harris, Criteria for cross-plane dominated thermal transport in multilayer thin film systems during modulated laser heating, J. Heat. Transf. 132 (8) (2010) 1–10.
[52] S. Shan, Z. Zhang, S. Lu, S. Volz, J. Chen, Generation of interfacial phonon modes and their contribution to thermal transport across the GaN/ZnO interface, Phys. Rev. B 112 (15) (2025) 155302.
[53] D. Li, A.J.H. McGaughey, Phonon dynamics at surfaces and interfaces and its implications in energy transport in nanostructured materials—an opinion paper, Nanoscale Microsc. Thermophys. Eng. 19 (2) (2015) 166–182.
[54] Q. Wang, C. Shao, Y. Xiong, S. Li, R. Wang, J. Sun, Y. Liu, X. Liu, Unlocking phonon dynamics at interfaces: angle-resolved transmission, mode conversion, and thermal conductance engineering, Int. J. Heat. Mass. Transf. 250 (2025) 127318.